UNIVERSITAT POLITÈCNICA DE CATALUNYA
BARCELONATECH
Escola d'Enginyeria de Telecomunicació
i Aeroespacial de Castelldefels

TREBALL DE FI DE GRAU

TFG TITLE: Active Flow Control of flow past SD7003 airfoil with Synthetic Jets at Re=60000

DEGREE: Bachelor's Degree in Aerospace Systems Engineering

AUTHOR: Pedro Muñoz Hoyos

ADVISOR: Dr.Fernando Pablo Mellibovsky Elstein

DATE: September 8, 2022

Títol: Active Flow Control of flow past SD7003 airfoil with Synthetic Jets at Re=60000
Autor: Pedro Muñoz Hoyos

Director: Dr.Fernando Pablo Mellibovsky Elstein

Data: 8 de setembre de 2022

Resum

Active Flow Control (AFC) és capaç de millorar notablement les capacitats aerodinàmiques de perfils alars. Centrant-se en una de les seves estratègies basada en l'ús d'actuadors de jet sintètics (SJA), el present treball de fi de grau estudia el rendiment de dos tipus de configuracions de jet sintètics a través d'un solver Reynolds-Averaged Navier-Stokes (RANS) capaç de tractar amb estats transitoris utilitzant tres models de turbulència diferents. La malla emprada per conduir els diferents estudis consisteix d'una malla C-type hibrida la qual va ser desenvolupada a través d'un programa python propi. El perfil alar considerat per aquest estudi és el Selig-Donovan 7003 (SD7003) en un angle d'atac $\alpha = 14^\circ$ en règim de post-stall a nombre de Reynolds $Re = 6 \cdot 10^4$. Un dels primers descobriments de l'estudi va ser que dos dels tres models de turbulència seleccionats, concretament $realizable - k - \varepsilon$ i $SST - k - \omega$, no eren capaços de resoldre correctament el flux en les condicions de post-stall del cas no actuat. A partir d'aquest punt, només el model Spalart-Allmaras ha sigut utilitzat per dur a terme els següents estudis dels diferents casos actuats. Per tal d'assegurar la veracitat dels resultats de l'estudi, aquests han sigut comparats amb la literatura disponible sempre que ha estat possible. El primer estudi va abordar la sensitivitat dels resultats obtinguts amb el model Spalart-Allmaras sobre la tria del valor de la condició de contorn de la viscositat turbulenta. Els resultats van concloure que existia una influència notable i que el valor que produïa els resultats més precisos quan aquests eren comparats amb resultats LES de la literatura era $\tilde{\nu}/\nu = 10^{-5}$. Seguidament, un estudi abordant el rendiment d'una implementació de jet tangencial per propòsits d'AFC va ser dut a terme simulant sis combinacions diferents de paràmetres SJA. A través dels resultats assolits es va concloure que la freqüència no dimensional F^+ jugava un paper crucial sobre l'estabilitat del camp de velocitat dins de la capa límit en aquest tipus de configuració jet. Finalment, l'estudi va mostrar resultats prometedors, ja que sis meres combinacions de paràmetres SJA van ser ja capaços de produir millores excepcionals sobre la sustentació i l'eficiència aerodinàmica del perfil alar.

Title : Active Flow Control of flow past SD7003 airfoil with Synthetic Jets at Re=60000
Author: Pedro Muñoz Hoyos

Advisor: Dr.Fernando Pablo Mellibovsky Elstein

Date: September 8, 2022

Overview

Active Flow Control (AFC) can improve markedly the aerodynamic capabilities of airfoils. Focusing on one of its strategies employing Synthetic Jet Actuators (SJA), the present bachelor thesis studied the performance of two synthetic jet configuration implementations via an unsteady Reynolds-Averaged Navier-Stokes (RANS) solver using three different turbulence models. The mesh employed to conduct the different studies consisted of a hybrid C-type grid which was developed via a hand-made python program. The airfoil considered was the Selig-Donovan 7003 (SD7003) in a post-stall angle of attack $\alpha = 14^\circ$ at Reynolds number $Re = 6 \cdot 10^4$. One of the first findings of the study was that two of the three selected turbulence models, concretely $realizable - k - \varepsilon$ and $SST - k - \omega$, failed to solve correctly the flow in the post-stall conditions of the baseline case. From that point on, only the Spalart-Allmaras model was used to conduct the following actuated studies. To ensure the veracity of the results obtained from the different baseline and actuated cases, they were compared to the available literature whenever possible. The first study addressed the sensitivity of the Spalart-Allmaras results on the boundary condition value chosen for the turbulent viscosity. Results concluded that a notable influence was present and that the value that produced the most accurate results when compared to LES ones from literature was $\tilde{\nu}/\nu = 10^{-5}$. Next, a study addressing the performance of a tangential jet implementation for AFC purposes was conducted by testing six different combinations of SJA parameters. From the obtained results was concluded that the non-dimensional frequency F^+ played a vital role in the stability of the velocity field within the boundary layer in this jet configuration. In addition, the study showed promising results as six mere combinations of different SJA parameters were already able of providing outstanding improvements on both the lift and aerodynamic efficiency of the airfoil.

to my family

CONTENTS

Introduction **1**

CHAPTER 1. Theory fundamentals **5**

1.1. Governing flow equations **5**

1.2. Turbulent flows **6**
  1.2.1. Random nature of turbulence 6
  1.2.2. Statistical approach 8

1.3. Mean-flow equations **8**
  1.3.1. Closure Problem 9

1.4. Turbulence models **10**
  1.4.1. Turbulent-viscosity hypothesis 10
  1.4.2. $k-\varepsilon$ model 10
  1.4.3. $k-\omega$ model 12
  1.4.4. Spalart-Allmaras model 12
  1.4.5. The law of the wall 13

1.5. Boundary layer theory **14**
  1.5.1. Boundary layer properties 15
  1.5.2. Flow separation 16
  1.5.3. Laminar and turbulent boundary layers 17
  1.5.4. Flow transition 18

CHAPTER 2. Numerical Setup **19**

2.1. Definition of the baseline and actuated cases **19**

2.2. Mesh construction **20**
  2.2.1. Mesh considerations 21
  2.2.2. Mesh Approaches 24

2.3. Flow solution **27**
  2.3.1. Flow solver 27
  2.3.2. Boundary conditions 27

2.4. Post-processing engine **29**

2.5. Convergence studies **30**

2.5.1. Mesh convergence study 30
2.5.2. Time step convergence study 32

CHAPTER 3. Results 35

3.1. Baseline case 35

3.2. Actuated cases 39
3.2.1. AFC parameters 40
3.2.2. Optimum SJA parameters 41
3.2.3. Tangential jet configuration 46

Conclusions 53

Bibliography 55

APPENDIX A. EXTRA AUDIOVISUAL MATERIAL 59

LIST OF FIGURES

1.1 x(t) time evolution ($\sigma = 10$, $\rho = 28$, and $\beta = 8/3$) for (a) the nominal (blue line) and perturbated (orange line) systems, and (b) the error between both. The time evolution has been obtained via numerical integration with $dt = 0.001$ s. 7

1.2 Dimensionless streamwise velocity profile in the vicinities of a body's surface (red line) and the tendencies of the viscous sub-layer and log-law region (blue lines). 14

1.3 Boundary layer and streamwise velocity profile. The dimensions of the boundary layer have been increased for clarity. 14

1.4 Development of an adverse pressure gradient (top) and evolution of the boundary layer velocity profile during the different stages that lead to separation (bottom). 16

1.5 Turbulent and laminar streamwise velocity profiles and their corresponding boundary layer thicknesses for a given chord position. 17

1.6 Transition process from a laminar to a turbulent boundary layer over a flat plate. x_{cr} stands for the critical location at which the flow can no longer be considered laminar and has to be considered turbulent instead. 18

2.1 Sketch of the computational domain and its different boundary regions, namely inlet (blue line), lower and upper regions (black lines), and outlet (red line). . . . 20

2.2 Memory storage mechanisms of both structured (left) and unstructured (right) cells. 21

2.3 Different degrees of orthogonality in cells placed in the vicinities of a wall. . . . 22

2.4 Different degrees of homogeneity in cell regions located in the vicinities of the inlet. 22

2.5 Cell skewness of two adjacent cell faces addressed through the angle θ. 23

2.6 Regions of cells containing different values of aspect ratio. 23

2.7 Illustration of the first mesh approach. The different mesh regions can be identified as far, mid, near, and closest regions by their respective distance from the inlet to the leading edge. 24

2.8 Illustration of the second mesh approach. Non-homogeneities can be easily spotted in the near region located in front of the leading edge. Additionally, in the wake closest regions, not only non-homogeneities can be noticed but also high aspect ratios. 25

2.9 (a) Illustration of the final mesh approach depicting the surrounding unstructured regions and its smooth transition of the cell resolution from the outer zones to the vicinities of the airfoil. (b) Close view of the closest region and the trailing edge section. (c) Close view of the closest region and its implementation of the synthetic jet section. 26

2.10 Mesh convergence study (a) pressure $C_p(x/C)$ and (b) skin friction $C_f(x/C)$ coefficient distributions and (c) a closer view of the skin friction coefficient distribution over the first half of the chord. 31

2.11 Time step convergence study skin friction coefficient $C_f(x/C)$ distributions with a x10 zommed section at $x/C = 0.3$ 33

3.1 Time evolution of the lift coefficient obtained with the (a) $realizable - k - \varepsilon$ and (b) $SST - k - \omega$ models. 35
3.2 Time evolution of the lift coefficient obtained with the Spalart-Allmaras model. . 36
3.3 Velocity field streamlines and turbulent viscosity contours of the baseline case obtained with the Spalart-Allmaras model. 37
3.4 Evolution of the upper-surface boundary layer velocity profile in the vicinities of the leading edge obtained with the Spalart-Allmaras model. 37
3.5 Baseline case (a) pressure $C_p(x/C)$ and (b) skin friction $C_f(x/C)$ coefficient distributions comparison with the literature. 38
3.6 Synthetic jet geometrical parameters. Oscillating membrane (orange line) not to scale. 40
3.7 Maximum lift configuration (a) pressure $C_p(x/C)$ and (b) skin friction $C_f(x/C)$ coefficient distributions from the several $\tilde{\nu}$ values. 43
3.8 Maximum efficiency configuration (a) pressure $C_p(x/C)$ and (b) skin friction $C_f(x/C)$ coefficient distributions from the several $\tilde{\nu}$ values. 44
3.9 Absolute optimum (a) pressure $Cp(x/C)$ and (b) skin friction $Cf(x/C)$ coefficient distributions comparison with the literature. 45
3.10 Tangential synthetic jet implementation into the airfoil's geometry. Oscillating membrane (orange line) not to scale. 46
3.11 Tangential synthetic jet auxiliary region (dark grey) and closest region (light grey) of the adapted mesh. 47
3.12 Maximum efficiency (red line), maximum lift (blue line), and baseline (green line) cases (a) pressure $Cp(x/C)$ and (b) skin friction $Cf(x/C)$ coefficient distributions. 49
3.13 Lift coefficient time evolution of the 'Actuated 3' case. 50
3.14 Destabilization of the boundary layer field caused by the fast production of recirculating regions across time units 23, 24, 25, and 26 pictured from top to bottom, respectively. 50

A.1 Tangential study maximum lift case streamlines evolution over an actuation period. 59
A.2 Tangential study maximum efficiency case streamlines evolution over an actuation period. 60

LIST OF TABLES

2.1 $Realizable-k-\varepsilon$ boundary conditions. 28
2.2 $SST-k-\omega$ boundary conditions. 29
2.3 Spalart-Allmaras boundary conditions. 29
2.4 Time-averaged aerodynamic performance parameters and mesh characteristics for the four different cases. 30
2.5 Time-averaged aerodynamic performance parameters, required time to reach convergence, and maximum Courant number reached on the converged solution for the four different cases. 33

3.1 Time-averaged aerodynamic performance coefficients of the baseline case and their respective errors with respect to the values found in the literature. 38
3.2 Maximized SJA parameters and its resulting mean aerodynamic performance coefficients obtained by Tousi et al. 41
3.3 Mean aerodynamic performance coefficients of the maximum lift SJA parameters across the several values of $\tilde{\nu}$. 42
3.4 Mean aerodynamic performance coefficients of the maximum aerodynamic efficiency SJA parameters across the several values of $\tilde{\nu}$. 42
3.5 Time-averaged aerodynamic performance coefficients of the absolute optimum and their respective errors with respect to the values found in the literature. . . 44
3.6 Mean aerodynamic performance coefficients of the actuated cases and lift and aerodynamic efficiency coefficient improvements with respect to the baseline case. 48

INTRODUCTION

The present study aims at using the Reynolds-Averaged Navier-Stokes (RANS) equations to study several active flow control (AFC) synthetic jet configurations and draw conclusions about their performance. For doing so, three turbulence models, namely $realizable-k-\varepsilon$, $SST-k-\omega$, and $Spalart-Allmaras$, are tested at baseline (unactuated) conditions to select the most appropriate one for the accurate prediction of the SD7003 airfoil aerodynamic performance in post-stall and actuated scenarios, concretely at $\alpha = 14^\circ$ and $Re = 6 \cdot 10^4$. The Selig-Donovan 7003 (SD7003) is a thin airfoil often employed in micro air vehicles (MAV). One of its particularities at moderate Reynolds numbers is that it develops a laminar separation bubble (LSB) on its suction side due to the strong adverse pressure gradient on its upper surface. As the angle of attack increases, the LSB moves towards the leading edge and reduces its length until the angle of attack reaches stall conditions, in which the flow does not reattach downstream, causing a large recirculation zone that dissolves the LSB.

Active flow control technology

Active flow control (AFC) technology is an extraordinary discipline capable of enhancing the aerodynamic performance of an airfoil by reducing its drag, increasing its lift, or increasing its overall aerodynamic efficiency. This technology consists of interacting with the boundary layer by means of exchanging momentum with the flow at particular locations of the airfoil so flow separation can be delayed, promoted, or even suppressed.

Increasing the aerodynamic performance of an airfoil can also be accomplished by means of passive flow control. Passive flow control introduces changes in the airfoil's geometry, like implementing vortex generators, so that the flow behaves as desired. One of the main disadvantages of this technique is that when the airfoil faces conditions different from those considered in the design phase, it can end up worsening the airfoil's aerodynamic performance.

Active flow control, on the other hand, is capable of increasing the aerodynamic performance of an airfoil in a broad range of conditions by adjusting its actuation parameters. However, it has its own downsides, as it needs external sources of energy to interact with the flow, which requires special care in assessing the energy balance in configurations like drag reduction or efficiency improvement. Proposed by Cattafesta and Sheplak [1], AFC strategies can be classified into three main classes: moving body actuators, plasma actuators, and fluidic actuators.

Starting with the former, moving body actuators induce local fluid motion by means of changing the body's geometry. This strategy can be thought of as the actuators on the control surfaces of an aircraft, in which by increasing their angle of attack they induce more or less aerodynamic lift or drag depending on the nature of the maneuver. Another type of actuation that has gained popularity in the last decade consists of plasma actuators. Plasma actuators interact with the boundary layer by means of ionized fluid jets. The on-growing popularity of these recent years can be attributed to the very fast time responses the ionized jets produce, which among other reasons, makes plasma actuators really appealing for aerodynamic applications.

Lastly, fluidic actuators, which are currently the most common approach, interact with the boundary layer by injecting/sucking fluid into/from it. Fluidic actuators can, at the same time, be divided into two families: zero net mass flow actuators (ZNMFA), also called synthetic jet actuators (SJA), and non-zero net mass flow actuators (NZMFA). The differentiating factor between the two comes from the origin/destination of the fluid. Non-zero net mass flow actuators require a source/sink of fluid to inject/suck fluid into/from the boundary layer, while zero net mass flow actuators do not require this source/sink to be present.

Focusing on synthetic jet actuators, which are the actuators employed in this study, they have been gaining popularity for the last two decades because of their simplicity and high capabilities for controlling flow separation. They consist of an oscillating membrane located on the airfoil's surface that sucks low-momentum fluid from the boundary layer as it oscillates towards its lowest point under the surface, and injects fluid with increased momentum into the boundary layer as it oscillates towards its highest position above the surface.

State of the art

Active flow control constitutes an active field of research in aerodynamics. For this reason, there is plenty of available literature on this topic, especially on airfoils. Fortunately, several studies have also been conducted on AFC over an SD7003 airfoil at $Re = 6 \cdot 10^4$. Such studies applied in most cases numerical methodologies ranging from Reynolds-averaged Navier-Stokes (RANS) models [2] [3] to Large eddy simulations (LES) [4] [5] [6].

Regarding RANS studies, Catalano and Tognaccini [3] conducted a numerical analysis over a large range of angles of attack from $\alpha = 0^\circ$ to $\alpha = 12^\circ$ with both RANS and LES approaches. By its own modifications of the well-known $SST - K - \omega$ model, they achieved results in good agreement with those of LES. On the other hand, Tousi et al. [2] optimized SJA-AFC actuation parameters over a range of four angles of attack, $\alpha = \langle 4^\circ, 6^\circ, 8^\circ, 14^\circ \rangle$, using genetic algorithms (GA). They concluded that as the angle of attack increases, the benefits of AFC become more pronounced, allowing considerable improvements in the airfoil's aerodynamic efficiency. Concretely, they obtained a maximum increase in the aerodynamic efficiency in post-stall conditions, $\alpha = 14^\circ$, of up to 251% with respect to the baseline case.

As for LES studies, Breuer [4] employed several inlet turbulence intensities to test their impact on the formation of the LSB at $\alpha = 4^\circ$. He concluded that high values for the inlet turbulence managed to reduce and even suppress the LSB, thereby enhancing the aerodynamic performance of the airfoil. Rodriguez et al. [5] applied SJA AFC across a range of pre-stall and post-stall angles of attack, $\alpha = \langle 4^\circ, 11^\circ, 14^\circ \rangle$, obtaining an aerodynamic efficiency increase of up to 124% for $\alpha = 14^\circ$, which also concluded that as the angle of attack increases the effect of AFC becomes more notable. Lastly, Tousi et al. [6] extended their previous RANS study [2] by assessing the accuracy of the previously thought optimized SJA parameters by comparing them with fully 3D LES results. They concluded that, although Spalart-Allmaras is not quite as accurate as LES, it can still predict useful macroscopic aerodynamic properties such as lift and drag coefficients, provided that the model parameters are properly adjusted.

Document structure

The structure of this document is composed of five parts. This very first part consisted of an introduction to the study's context through a brief insight into Active flow control (AFC) and its state of the art on the SD7003 airfoil.

The second part, which makes the first chapter of the document, aims at providing the reader with most of the knowledge required for conducting this study. It takes the reader from an introduction to turbulent flows, their statistical treatment, and modeling to boundary layer theory necessary for a better understanding of active flow control.

The third part depicts the build-up of the numerical setup required for conducting the simulations. In this third part, the computational domain, its boundary conditions, the mesh construction process, and the software employed are presented. In addition, two convergence studies of both the mesh and the time-step are conducted to choose and validate their quality for their use in the rest of the study.

The fourth part presents all the results obtained from different simulations carried out during the study. Firstly, it shows the analysis and comparison with the literature of the baseline case results. Later on, it exposes the several actuated studies conducted, their specific numerical setup, their analysis, and their comparison with the corresponding literature whenever this was possible.

To conclude, the fifth part presents the conclusions drawn from the study together with some proposals about possible future lines of work.

CHAPTER 1. THEORY FUNDAMENTALS

This chapter aims at reviewing some of the most important theoretical concepts relevant to the study. The chapter thread is based on leaving the reader with an understanding of turbulent flows, their governing equations, their statistical nature, their modeling, and boundary layer theory. This chapter tries to avoid digging deep into concepts that are not essential for this work's purposes and cites the sources of information consulted by the author where further explanations can be found.

1.1. Governing flow equations

In fluid mechanics, as in any other scientific field of study, theories and mathematical models are based upon axioms. An axiom, or equivalently a postulate or assumption, states a certainty upon which further reasoning can be elaborated. When it comes to fluids, the three following axioms lead to the fundamental governing equations of fluid motion.

- Mass is conserved
- Fluid particles fulfill Newton's second law
- Energy is conserved

Each of these postulates leads to a governing equation - namely the mass conservation equation (or continuity equation), the momentum equation, and the energy equation. Deriving and interpreting these equations in terms of control volumes and fluid particles is an extraordinary way of understanding most of the physical phenomena present in flows. However, as these derivations can become rather extensive, they will not be made here - for such detailed derivations, see [7] and [8]. Additionally, for this study's purposes, the energy equation will not be considered, as the thermal behavior of the flow is not within the scope of this study.

The first of the remaining two governing equations is the mass conservation equation, which takes the following form:

$$\frac{\partial \rho}{\partial t} + \nabla \cdot (\rho U) = 0 \tag{1.1}$$

It is straightforward to see that if the flow is incompressible, it yields simply to the condition of the flow velocity field being divergence-free. On the other hand, the momentum equation, best known in the world of fluid mechanics as the Navier-Stokes equations, take the following form:

$$\frac{\partial U}{\partial t} + (U \cdot \nabla) U = -\frac{1}{\rho} \nabla p + \nu \nabla^2 U \tag{1.2}$$

If the flow were to be inviscid, the Navier-Stokes equations would result in the flow being driven only by pressure gradients, as viscosity processes would no longer be present. In that case, the previous two equations would take their name after Euler, honoring his formulation of the governing flow equations for inviscid flows.

Another key characteristic to notice from the momentum equation is that it is a vector equation. Therefore, equation 1.2 can be expanded into three different equations, one for each spatial component. Nevertheless, to avoid dealing with numerous equations resulting from this vectorial nature, they are often expressed through the Einstein summation convention, also known as suffix notation. By applying this convention, the governing equations are rewritten as:

$$\frac{\partial \rho}{\partial t}+\frac{\partial\left(\rho U_i\right)}{\partial x_i}=0 \tag{1.3}$$

$$\frac{\partial U_j}{\partial t}+U_i\frac{\partial U_j}{\partial x_i}=-\frac{1}{\rho}\frac{\partial p}{\partial x_j}+\nu\frac{\partial^2 U_j}{\partial x_i \partial x_i} \tag{1.4}$$

This last set of equations, formed by the continuity and momentum equations, have four unknowns, namely the three components of the velocity field and the pressure. Therefore, as it has the same number of equations as unknowns, it is said to be closed. As will be seen in the following sections, the concept of closure becomes critical when dealing with turbulent flows.

1.2. Turbulent flows

Turbulent flows can be spotted almost everywhere, the smoke from a chimney, the contrails made by an aircraft, or even the water of a sink, turbulence is present in all of them. If stopped to look at them for a moment, some common traits could be easily recognizable; its flow is unsteady, irregular, and chaotic.

For many, these traits would be enough to find turbulent flows interesting. However, they are also of paramount importance for many engineering applications, as chaotic motion allows mixing fluid properties far more effectively than ordered motion does. Therefore, it is not surprising to see both industry and academia making efforts to understand and exploit turbulence at a deeper level.

1.2.1. Random nature of turbulence

The velocity field $U(x,t)$ of turbulent flows is random. At first glance, this might seem like an inconsistency between the deterministic nature of classical mechanics, embodied in the Navier-Stokes equations, and the seemingly random behavior of turbulent flows. Nevertheless, this phenomenon can be easily explained via two observations:

- Turbulent flows are subjected to numerous perturbations.
- Turbulent flows display extreme sensitivity to these perturbations.

To better understand what a perturbation is, consider a fluid-flow experiment that can be reproduced under the same set of nominal conditions, for example, a flow of water through a pipe of 10 cm of diameter at 20 ºC. It results rather obvious that these two conditions only are not enough to fully characterize the set of conditions in which the experiment is being carried out. However, no matter how much effort is put into defining a set of nominal conditions, the experiment will never be fully characterized. The reason is simple, in practice, inevitably, there are unknown vibrations, tiny irregularities in the body's surfaces, impurities, inhomogeneities in the flow properties, etc., that cannot be included when defining the experiment.

However, the presence of perturbations does not fully describe the random nature of turbulent flows by itself, as they are also present in laminar flows. The difference is that, at the turbulent flows' high Reynolds numbers, the evolution of the flow becomes extremely sensitive to these small changes. Such sensitivity can be well understood via the Lorenz equations. Edward Lorenz proposed a system characterized by three state variables $[x(t), y(t), z(t)]$, which evolve accordingly to the following set of deterministic ordinary differential equations.

$$\begin{aligned} \dot{x} &= \sigma(y - x) \\ \dot{y} &= \rho x - y - xz \\ \dot{z} &= -\beta z + xy \end{aligned} \tag{1.5}$$

Consider the time evolution of the system with initial conditions $[x(0), y(0), z(0)] = [0.1, 0.1, 0.1]$, and compare it to the same system but with a perturbation of 10^{-6} in $x(0)$- that is $[x(0), y(0), z(0)] = [0.100001, 0.1, 0.1]$. Even though the system behaves quite similarly for the first 30 seconds, the perturbation has a clear effect on its behavior from this point on, as can be seen in figure 1.1. Consequently, if the initial conditions are known only within 10^{-6} of accuracy, no useful long-term predictions can be made about the system's behavior. Therefore, Lorenz equations prove how a simple set of deterministic equations, much simpler than the Navier-Stokes, can display an acute sensitivity to perturbations that result in unpredictability. This phenomenon is known as deterministic chaos, and even though no precise long-term predictions can be made in most cases, as will be seen in the following section, statistical treatment provides an alternative approach to deal with these types of equations.

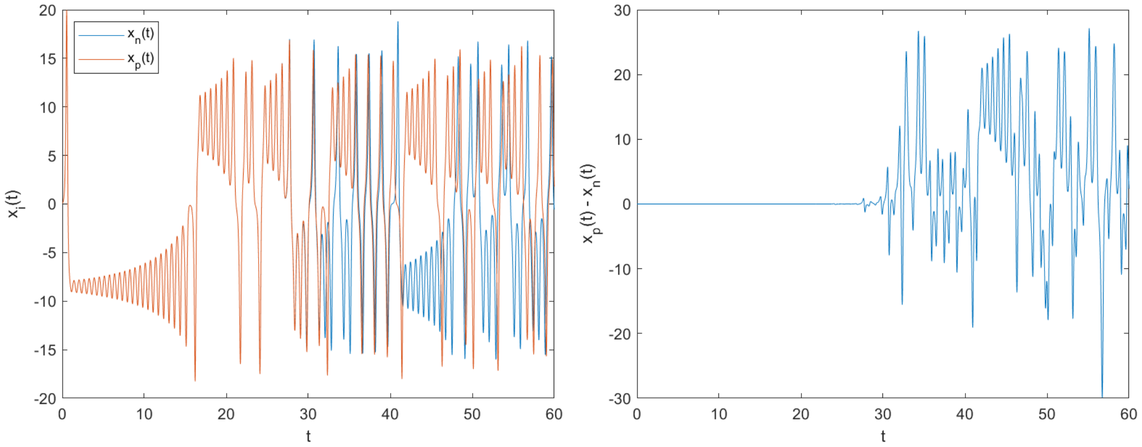

(a)

(b)

Figure 1.1: x(t) time evolution ($\sigma = 10$, $\rho = 28$, and $\beta = 8/3$) for (a) the nominal (blue line) and perturbated (orange line) systems, and (b) the error between both. The time evolution has been obtained via numerical integration with $dt = 0.001$ s.

But there is more, the qualitative behavior of the system depends also on the coefficients (σ, ρ, β). In particular, for fixed values of σ = 10, and β = 8/3, if ρ is less than a critical value $\rho^* \approx 24.74$, then the system converges to fixed values of $[x(t), y(t), z(t)]$. However, for $\rho > \rho^*$, chaotic behavior arises. Again, this is similar to what happens with the Navier-Stokes equations, which have ordered laminar solutions at sufficiently low Reynolds numbers, but chaotic turbulent solutions at higher Reynolds numbers. In fact, such sensitivities are common in many engineering disciplines and constitute an active field of study in dynamical systems and chaos theory.

1.2.2. Statistical approach

Despite seeing how the Navier-stokes equations can be extremely sensitive to perturbations, yielding to unpredictability due to the lack of ability to fully characterize a flow experiment, it does not make them any less convenient.

For laminar flows, Navier-Stokes equations can still be used to calculate values of the velocity field $U(x,t)$, perform an experiment to measure this velocity field, and from past experiences, there is a high degree of confidence that the numerically computed values and the experimental measurements will agree (to within small numerical and experimental tolerances).

Turbulent flows, on the other hand, can be studied by solving the Navier-Stokes equations numerically. This approach is called direct numerical simulation, commonly known as DNS. It allows researchers to study turbulence in detail as they are able to analyze the different stages and scales of turbulence. Unfortunately, this approach is very computationally demanding, which limits its applicability. Alternatively, Turbulent flows are solved frequently in academia via Large Eddy Simulation or LES, which consists of filtering small turbulent scales and solving again the Navier-Stokes equations so that the computational time required to obtain a solution is notoriously reduced. However, this reduction in computational time comes at the cost of a certain degree of accuracy in the solutions. Lastly, to reduce even further the computational requirements, which is paramount for some engineering purposes, the Navier-Stokes equations can be treated statistically, which leads to the different turbulence models, as will be seen in the following sections. Similarly to LES, this further reduction in computational resources comes at the expense of accuracy.

1.3. Mean-flow equations

The statistical treatment of the Navier-Stokes equations is extremely useful for engineering purposes. Many engineering flow problems are notoriously complex, and the computational cost associated with its study via LES or DNS is, in most cases, prohibitive. For this reason, the reduction of the computational requirements that statistical treatment brings with it is of paramount interest to engineering purposes.

The most basic way of applying statistics to the Navier-Stokes equations is to look at the velocity field $U(x,t)$ as the sum of its means value $\langle U(x,t) \rangle$ and a fluctuation $u(x,t)$. Firstly proposed by Reynolds, this approach is often referred to as the Reynolds decomposition.

$$U(x,t) = \langle U(x,t) \rangle + u(x,t) \tag{1.6}$$

Furthermore, by taking the mean of the Navier-Stokes equations and applying the Reynolds decomposition, the mean continuity and momentum equations are formulated. This process is not shown in this chapter as it can be rather extensive - for a detailed derivation of these equations see [9]. Lastly, this set of new mean equations takes the name of Reynolds-Averaged Navier-Stokes, commonly known as RANS equations.

$$\frac{\partial\langle U_i\rangle}{\partial x_i}=0 \tag{1.7}$$

$$\frac{\partial\langle U_j\rangle}{\partial t}+\langle U_i\rangle\frac{\partial\langle U_j\rangle}{\partial x_i}=\nu\frac{\partial^2\langle U_j\rangle}{\partial x_i^2}-\frac{1}{\rho}\frac{\partial\langle p\rangle}{\partial x_j}-\frac{\partial\langle u_iu_j\rangle}{\partial x_i} \tag{1.8}$$

RANS and Navier-Stokes equations are quite similar, except for the velocity covariances term $\langle u_iu_j\rangle$, which are often referred to as the Reynolds stresses. Reynold stresses $\langle u_iu_j\rangle$ play a crucial role in the mean velocity field $\langle U(x,t)\rangle$. Were $\langle u_iu_j\rangle$ to be zero, the equations for $\langle U(x,t)\rangle$ and the Navier-Stokes equations would be the same. Therefore, the very different behavior of the random velocity field $U(x,t)$ and the mean velocity field $\langle U(x,t)\rangle$ can be associated with the Reynolds stresses' presence. Rewriting the mean momentum equation can be very useful to give an insight into the effect of the Reynolds stresses in the flow.

$$\rho\frac{\partial\langle U_j\rangle}{\partial t}+\rho\langle U_i\rangle\frac{\partial\langle U_j\rangle}{\partial x_i}=\frac{\partial}{\partial x_i}\left[\mu\left(\frac{\partial\langle U_i\rangle}{\partial x_j}+\frac{\partial\langle U_j\rangle}{\partial x_i}\right)-\langle p\rangle\delta_{ij}-\rho\langle u_iu_j\rangle\right] \tag{1.9}$$

This form of formulating the mean momentum equation contains within its brackets the sum of three stresses, namely viscous stress from the friction forces, isotropic stress from the mean pressure field $-\langle p\rangle\delta_{ij}$, and the apparent stress caused by the fluctuating velocity field $-\rho\langle u_iu_j\rangle$. Even though the apparent stress consists of $-\rho\langle u_iu_j\rangle$, it is common practice to refer to $\langle u_iu_j\rangle$ as the Reynolds stress. Therefore, the Reynold stress can be visualized as the mean momentum transfer caused by the fluctuating velocity field $u(x,t)$. In addition, the trace of the Reynolds stresses defines the turbulent-kinetic energy, which expresses the mean kinetic energy per unit mass associated with the fluctuating velocity field $u(x,t)$. As will be seen in the following section, it is a vital parameter when it comes to turbulence modeling.

$$k=\frac{1}{2}\langle u_iu_i\rangle \tag{1.10}$$

1.3.1. Closure Problem

For a general three-dimensional turbulent flow, there are four independent equations governing the mean velocity field $\langle U(x,t)\rangle$; the three components of the mean momentum equation and the mean continuity equation. However, these four equations contain more than four unknowns. Besides $\langle U(x,t)\rangle$ and $\langle p(x,t)\rangle$ (four quantities), there are also the Reynolds stresses $\langle u_iu_j\rangle$, which cause the mean-flow equations to be undetermined.

When a set of equations contains more unknowns than independent equations, it is said to be unclosed. Therefore, to close the set of equations and characterize all the unknowns, additional information is required. In the case of RANS equations, the Reynolds stresses constitute the extra unknowns, and unless they are somehow determined, RANS equations cannot be solved.

1.4. Turbulence models

With the aim of closing the RANS equations, the Reynolds stresses are determined via several hypotheses or models. In the case of the turbulence models selected to conduct this study, the hypothesis upon which they are developed is the turbulent-viscosity hypothesis.

1.4.1. Turbulent-viscosity hypothesis

The turbulent-viscosity hypothesis serves as a source of additional information to close the RANS equations. Originally proposed by Boussinesq, it relates the Reynolds stresses with the mean rate of strain via the following equation:

$$-\rho\langle u_i u_j\rangle = \mu_T\left(\frac{\partial\langle U_i\rangle}{\partial x_j}+\frac{\partial\langle U_j\rangle}{\partial x_i}\right)-\frac{2}{3}k\rho\delta_{ij} = 2\mu_T\overline{S}_{ij}-\frac{2}{3}k\rho\delta_{ij} \tag{1.11}$$

where $\nu_T(x,t)$ is the turbulent viscosity, often called eddy viscosity. This equation aims to recreate a relationship between the Reynolds stresses and the mean rate-of-strain tensor similar to the viscous stress relationship with the rate-of-strain in Newtonian fluids.

$$\tau_{ij} = 2\mu S_{ij} - P\delta_{ij} \tag{1.12}$$

The turbulent-viscosity hypothesis can be viewed as two different assumptions. Firstly, the intrinsic assumption, states that for every (x,t), the Reynolds stresses modify the local mean rate of strain. Secondly, the specific assumption, states that the local mean rate of strain is related to the Reynold stresses specifically as shown in equation 1.11.

Unfortunately, for some flows the accuracy of the hypothesis is poor, and other turbulence modeling approaches have to be taken - for further details about the flaws of the turbulent-viscosity hypothesis see [9]. Nevertheless, were the turbulent-viscosity hypothesis to be adequate for a given flow, as is the case of this study, all that would remain to be done to close the RANS equations would be determining the turbulent viscosity $\nu_T(x,t)$. Precisely for this last matter is that RANS turbulence models were developed.

1.4.2. $k-\varepsilon$ model

The $k-\varepsilon$ model aims to obtain the turbulent viscosity $\nu_T(x,t)$ via two turbulence quantities, namely the turbulent-kinetic-energy k, and the turbulent-kinetic-energy dissipation rate ε. The model is classified as a two-equation model, as it obtains the two previous turbulent properties by solving two different transport equations.

The first transportation equation of the model concerns the turbulent kinetic energy. This transport equation comes from the mean substantial derivative of such property, which after some mathematical treatment, results in the following equation:

$$\frac{\overline{D}k}{\overline{D}t} = \nabla \cdot \left(\frac{\nu_T}{\sigma_k} \nabla k \right) + P - \varepsilon \tag{1.13}$$

where σ_k is the turbulent Prandtl number for kinetic energy and P is the rate of production of turbulent kinetic energy. Physically, P represents the rate at which turbulent flow motion is being induced due to the flow's turbulent kinetic energy. In contrast, the ε transport equation, rather than being derived entirely analytically, is best defined via empirical observations, which lead to the following equation:

$$\frac{\overline{D}\varepsilon}{\overline{D}t} = \nabla \cdot \left(\frac{\nu_T}{\sigma_\varepsilon} \nabla \varepsilon \right) + C_{\varepsilon 1} \frac{P\varepsilon}{k} - C_{\varepsilon 2} \frac{\varepsilon^2}{k} \tag{1.14}$$

where $C_{\varepsilon 1}$ and $C_{\varepsilon 2}$ are two of the five model parameters, and σ_ε is the turbulent Prandtl number for the kinetic energy dissipation rate. Keeping in mind that obtaining the turbulent viscosity field is the ultimate goal of the model, $\nu_T(x,t)$ is calculated as a function of the solved turbulent quantities k and ε with the following expression:

$$\nu_T(x,t) = C_\mu \frac{k(x,t)^2}{\varepsilon(x,t)} \tag{1.15}$$

The derivation of the previous expression is grounded on empirical observations and turbulent length scales - for further details about its derivation see [9] and [10]. Lastly, in order to finally be able of solving turbulent flows, the model constants have to be determined. It is straightforward to see that the values that these constants take are fundamental to the integrity of the model's results, as wrong values would produce meaningless solutions. For this reason, many efforts have been made to obtain adequate values for the different model parameters. Rising from these efforts, Launder and Sharma defined what are considered to be the standard values for the $k-\varepsilon$ model, namely:

$$C_\mu = 0.09, \quad C_{\varepsilon 1} = 1.44, \quad C_{\varepsilon 2} = 1.92, \quad \sigma_k = 1, \quad \sigma_\varepsilon = 1.3 \tag{1.16}$$

Nevertheless, these values represent a compromise, and it is almost certain that for any particular flow the accuracy of the model results can be enhanced by tuning these values. However, if these were to be adjusted, these same parameters would likely perform poorly in any other flow scenario than the standard values would do. For this reason, the standard values depicted in 1.16 provide an overall reasonable performance for an extensive range of flows.

The $k-\varepsilon$ model is arguably the simplest complete turbulence model, and it is precisely because of its simplicity that it has the widest range of applicability, as no severe restrictive assumptions are made during its formulation. One of its major drawbacks is that it requires several modifications in its transport equations in order to be used on viscous near-wall regions. However, this issue can be easily overcome by using hybrid models, as will be seen in the following section.

1.4.3. $k-\omega$ model

Similar to the $k-\varepsilon$, the $k-\omega$ model is a two-equation model that obtains the turbulent viscosity $\nu_T(x,t)$ via two turbulence quantities. The first of which is again the turbulent kinetic energy k solved via the same transport equation seen in the $k-\varepsilon$ model 1.13. Based on empirical observations, Kolmogorov and Prandtl suggested that it would be desirable to define the turbulent viscosity in terms of the turbulent kinetic energy. As a result, many two-equation models solve one of their transport equations for k.

Regarding the second transport equation, there can be different choices for the objective turbulent property. Proposed by Kolmogorov, the $k-\omega$ model solves the second transport equation for the turbulent specific dissipation rate ω, while the model proposed by Saffman solves it for ω^2. Nowadays, the standard $k-\omega$ model consists of the one developed by Willcox, where $\omega \equiv \varepsilon/k$ is solved via the following transport equation:

$$\frac{\bar{D}\omega}{\bar{D}t} = \nabla \cdot \left(\frac{\nu_T}{\sigma_\omega} \nabla \omega \right) + (C_{\varepsilon 1} - 1)\frac{P\omega}{k} - (C_{\varepsilon 2} - 1)\omega^2 + \frac{2\nu_T}{\sigma_\omega k} \nabla \omega \cdot \nabla k \tag{1.17}$$

Note that as ω is defined in terms of ε, the definition of $\nu_T(x,t)$ in equation 1.15 still holds, and thus no additional assumptions are required. This standard $k-\omega$ model gives an accurate treatment of the viscous near-wall region, which was precisely where the $k-\varepsilon$ model was most vulnerable. However, its treatment of non-turbulent free-stream boundaries results problematic, as a non-physical boundary condition on ω is required leading to the calculated flow being highly sensitive to this value.

Arguably not purely a $k-\omega$ model, Mender proposed a two-equation hybrid model accounting for the best behavior of the $k-\varepsilon$ and $k-\omega$ models. It is not surprising, therefore, that this two-equation model has become one of the most used by the industry. Taking the name of $SST-k-\omega$ model, where SST stands for shear stress transport, it contains a blending function in the last term of equation 1.17. This blending function makes the model behave as the standard $k-\omega$ model close to the walls, while it switches to the standard $k-\varepsilon$ model away from the walls. For this promising feature, the $SST-k-\omega$ model is the second turbulence model chosen for this study.

1.4.4. Spalart-Allmaras model

Contrary to the previous two-equation models, Spalart and Allmaras developed a one-equation model specifically for aerodynamic applications. In this model, the turbulent viscosity $\nu_T(x,t)$ is determined directly via the one transport equation shown in 1.18. The derivation of this transport equation and the details of the model are remarkably complex, and no further elaboration about its terms will be made - for further insight into the model details, see [11].

$$\frac{\bar{D}\nu_T}{\bar{D}t} = \nabla \cdot \left(\frac{\nu_T}{\sigma_\nu} \nabla \nu_T \right) + S_\nu \tag{1.18}$$

It is interesting to see that despite the Spalart-Allmaras model being a one-equation model, which could seem like a drawback when comparing it to two-equation models, it is able to produce results with a high degree of accuracy. The reason for this to happen is related to the model being developed only for aerodynamic flows. Rather than fully capturing the turbulent behavior of a broad range of turbulent flows, the Spalart-Allmaras model aims to capture only the turbulent behaviors present in aerodynamic flows. As a result, despite employing only one transport equation, the Spalart-Allmaras model is able to outperform two-equation models, which are intended to be of general application, in the type of flows for which it has been designed. Therefore, far to serve as a general model, as it would likely produce poor results when taken outside of aerodynamic applications, it makes a perfect candidate for solving turbulent aerodynamic flows. Consequently, as it matches perfectly with the context of the study, the Spalart-Allmaras model is the third model selected to perform the upcoming simulations.

1.4.5. The law of the wall

Despite turbulent flows being characterized by chaotical behaviors, when dimensional analysis is applied to the vicinities of a body's surface, it shows that the flow in this region depends only on the surface characteristics, no matter the outer flow conditions. Taking the name of the law of the wall, this phenomenon becomes crucial when simulating turbulent flows. The two dimensionless variables that are essential to formulate this law are the dimensionless length y^+ and the dimensionless velocity u^+. Defined by the following expressions, these variables characterize the wall conditions that govern the flow behavior in this region.

$$y^+ = \frac{y}{\nu}\left(\frac{\tau_w}{\rho}\right)^{\frac{1}{2}} \qquad u^+ = u\left(\frac{\tau_w}{\rho}\right)^{-\frac{1}{2}} \tag{1.19}$$

Similarly to many other fluid mechanics flow quantities, the vertical velocity profile near the wall $u(y)$ can be normalized so that it becomes $u^+(y^+)$. Shockingly, in contrast to the dimensional velocity profile $u(y)$, the normalized velocity profile $u^+(y^+)$ is found to have the same distribution in almost all turbulent flows near a body's surface. The law of the wall holds in the first three regions right next to a surface, namely, the viscous sublayer, the buffer layer, and the log-law region. In figure 1.2, these three regions can be easily identified by their $u^+(y^+)$ trends. The viscous sublayer is characterized by u^+ increasing proportionally to (y^+), the log-law region by the logarithmic dependence of u^+ on (y^+), and the buffer layer by acting as a transition zone between these two trends. Note that the y^+- axis is on a logarithmic scale.

One of the main reasons why the law of the wall is so vital for simulating turbulent flows is that it can serve as a model for the velocity profile near a wall for flow solvers. This modeling near a wall is what is commonly known as wall functions. Wall functions aim to act as a bridge between the inner region, shown in figure 1.2, and the fully developed turbulent region. Unfortunately, as each turbulence model solves the flow in a different manner, they must use different wall functions and require the y^+ coordinate of the first cell layer adjacent to the wall to lie in different ranges. For this last reason, the $k-\varepsilon$ specific model employed during the study is the $realizable-k-\varepsilon$ model. This specific model requires similar values of y^+ for the mesh's closest nodes to the wall than $SST-k-\omega$ and Spalart-Allmaras, which allows using a single mesh for the three models.

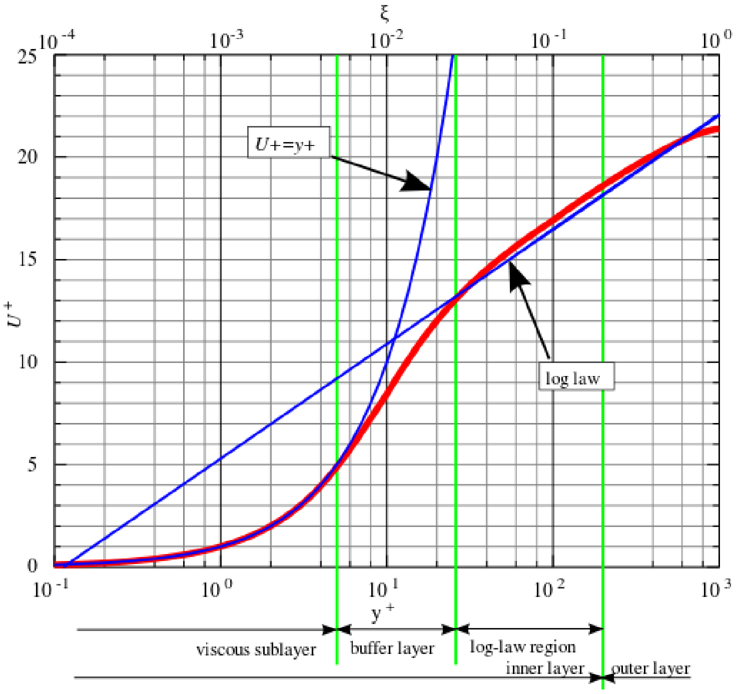

Figure 1.2: Dimensionless streamwise velocity profile in the vicinities of a body's surface (red line) and the tendencies of the viscous sub-layer and log-law region (blue lines). [12]

1.5. Boundary layer theory

Since AFC consists of exchanging momentum with the boundary layer, being familiar with its theory will allow comprehending better some of the actuated cases' results. The concept of boundary layer was first introduced by Prandtl in the early 20th century. Prandtl noticed that for viscous flows, the region away from the body seemed to be frictionless and had relatively small velocity gradients. On the other hand, in the vicinities of the body, large velocity gradients were present and friction seemed to play a crucial role in the flow behavior. This last region is what is currently known as the boundary layer. For most flows of interest, despite the boundary layer being very thin compared with the rest of the flow scales, its impact on the flow behavior is significant.

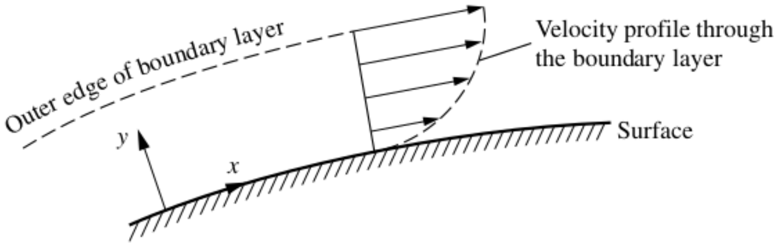
Outer edge of boundary layer
Velocity profile through the boundary layer
Surface
y
x

Figure 1.3: Boundary layer and streamwise velocity profile. The dimensions of the boundary layer have been increased for clarity. [13]

To better comprehend the concept of boundary layer, it is useful to visualize air flowing over an airfoil as shown in figure 1.4. Due to friction, the layer of air molecules adjacent to the airfoil's surface sticks to the surface resulting in their relative velocity being zero - the famously known *no-slip* condition. In contrast, at some point in the surface normal's direction, there is a layer of air moving relative to the airfoil as if friction was nonexistent. As a result, the region in between where the air goes from having zero relative velocity to moving as if the flow was inviscid, marks the region where friction forces govern the flow behavior, or in other words, the boundary layer.

1.5.1. Boundary layer properties

It is interesting to introduce some properties related to the boundary layer that prove useful in flow analysis. The first one consisting of the velocity boundary-layer thickness δ_{99}, it is by definition, the distance above the wall where the flow velocity reaches $0.99u_{inviscid}$, so that, for a given *x*-chord position, $u(\delta_{99}) = 0.99u_{inviscid}$. It is important to notice that the boundary layer thickness δ_{99} varies across the chord $\delta_{99} = \delta_{99}(x)$, normally being the smallest at the leading edge and increasing in the positive streamwise direction. The second boundary layer property is the displacement thickness δ^*, which is defined via the following expression:

$$\delta^* \equiv \int_0^{y_1} \left(1 - \frac{\rho u}{\rho_e u_e}\right) dy \qquad \delta_{99} \leq y_1 \tag{1.20}$$

To better comprehend this property, consider an inviscid flow passing through a section perpendicular to a surface so that there exists a mass flow. Similarly, consider a viscous flow passing through the same section. As the flow velocity goes from zero to its inviscid value, it is straightforward to see that there has been a reduction in the mass flow through the section with respect to the inviscid case. In light of this, the displacement thickness δ^* can be physically considered as the height increase of the body's surface so that the mass flow of an inviscid flow and the mass flow of a viscous flow going over the original non-increased surface are the same. Alternatively, it also can be conceived as the height of a hypothetical inviscid flow stream tube carrying the missing mass flow due to the viscous velocity blockage at the boundary layer. Similarly, the momentum thickness θ, defined via the following expression:

$$\theta \equiv \int_0^{y_1} \frac{\rho u}{\rho_e u_e} \left(1 - \frac{u}{u_e}\right) dy \qquad \delta_{99} \leq y_1 \tag{1.21}$$

Is equivalent in its physical meaning to the displacement thickness, but rather than the missing mass flow, it represents the missing momentum flow due to the viscous velocity blockage. Again, it is important to notice that, just like the boundary layer thickness, both the displacement thickness and the momentum thickness vary across the chord $\delta^* = \delta^*(x)$ and $\theta = \theta(x)$.

Lastly, the wall shear stress τ_w constitutes a fundamental property in both aerodynamics and boundary layer theory. The wall shear stress quantifies the skin friction over the body's surface, which is proportional to the wall-normal gradient of the streamwise velocity present within the boundary layer. In addition, like with many other fluid mechanics properties, its non-dimensional value, the skin friction coefficient c_f, is commonly used to characterize the same phenomenon. These two properties are formulated mathematically through the following expressions:

$$\tau_w = \mu \left(\frac{\partial u}{\partial y} \right)_w \tag{1.22}$$

$$c_f = \frac{\tau_w}{\frac{1}{2}\rho_e U_e^2} \tag{1.23}$$

where μ is the dynamic viscosity of the fluid, ρ_e the fluid density at the edge of the boundary layer, and U_e the velocity at at the edge of the boundary layer.

1.5.2. Flow separation

The phenomenon of flow separation is arguably one of the most relevant concepts for this study. Separation occurs due to the presence of severe adverse pressure gradients over a body's surface. To better comprehend this phenomenon imagine a flow over an airfoil's upper surface. When the flow reaches the leading edge, it encounters the stagnation point and starts increasing its velocity quickly as it moves in the streamwise direction, until at some point in the middle section of the airfoil, it starts decreasing again. In contrast, consider this very same process but from the perspective of the flow pressure. As the flow decelerates across the positive streamwise direction, its pressure starts increasing, giving, as a result, a positive pressure gradient in the streamwise direction. The sharper the deceleration caused by the airfoil's geometry or the angle of attack, the more severe the pressure gradient.

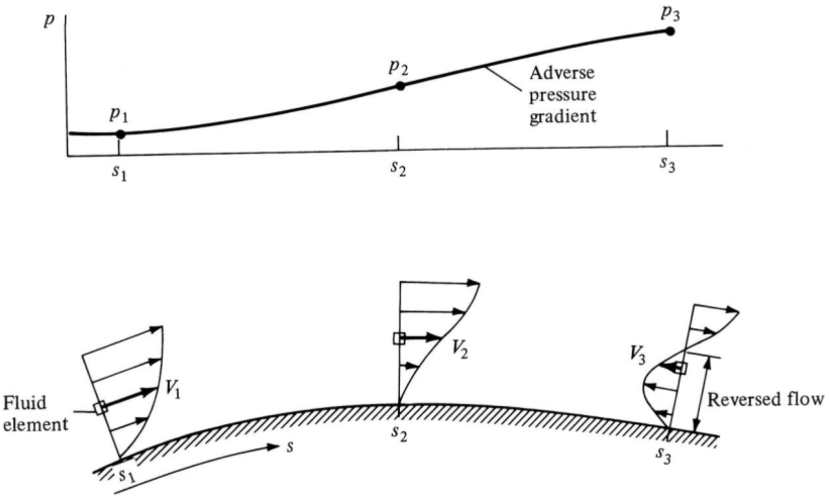

Figure 1.4: Development of an adverse pressure gradient (top) and evolution of the boundary layer velocity profile during the different stages that lead to separation (bottom). [13]

Severe pressure gradients often have no effect on the fluid elements outside the boundary layer as they possess high kinetical energy. However, as fluid elements within the boundary layer have less velocity due to viscous blockage, positive severe pressure gradients in the streamwise direction can end up stopping and even reversing the direction of the flow within the boundary layer. This reversion in the flow's direction is what is known as separation. This last process seen from the pressure point of view is depicted in figure 1.4.

Flow separation leads to two major drawbacks in the aerodynamic performance of an airfoil. Firstly, there is a drastic loss of lift, commonly known as stalling, caused directly by the rising pressure on the final section of the upper surface. Secondly, pressure drag appears embodied in a net pressure force acting in the streamwise direction due to the pressure on the trailing edge being lower than on the leading edge.

To conclude, locating where separation occurs is a very interesting task for flow analysis. Following the previous reasoning, this point can be directly obtained by looking at the skin friction coefficient distribution. As the flow is stopped and reversed during separation, the separation point aligns with the location where the skin friction coefficient changes its sign.

1.5.3. Laminar and turbulent boundary layers

As mentioned in the previous sections, laminar and turbulent flows behave substantially differently. Therefore, it should not be surprising that laminar and turbulent boundary layers also possess marked differences. One of these differences is that the boundary layer thickness δ_{99} is bigger in turbulent boundary layers than in laminar ones. As a consequence, their velocity profiles through the boundary layer evolve differently. As shown in figure 1.5, turbulent velocity profiles maintain a close free-stream value during most parts of the boundary layer until quickly decreasing to zero at the surface. This behavior results in a ”fuller” velocity profile when compared to the one of a laminar boundary layer.

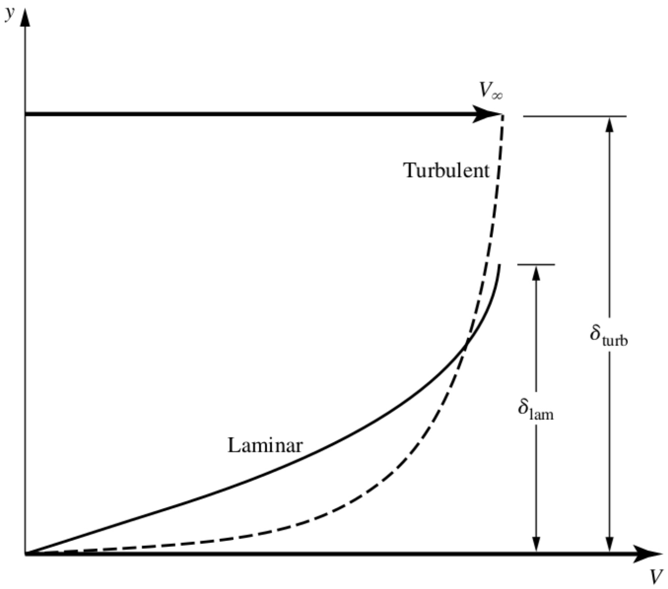

Figure 1.5: Turbulent and laminar streamwise velocity profiles and their corresponding boundary layer thicknesses for a given chord position. [13]

Such differences between both velocity profiles lead to very interesting consequences on their boundary layer properties. As the velocity gradient near the wall is bigger in turbulent boundary layers, it is straightforward to see by looking at the wall shear stress definition 1.22, that for the same boundary layer thickness $\delta_{99}^{laminar} = \delta_{99}^{turbulent}$, turbulent boundary layers result in higher values of the skin friction coefficient.

$$\left(\frac{\partial u}{\partial y}\right)_w^{laminar} < \left(\frac{\partial u}{\partial y}\right)_w^{turbulent} \tag{1.24}$$

$$\tau_w^{laminar} < \tau_w^{turbulent} \tag{1.25}$$

Alternatively, as turbulent velocity profiles are ”fuller”, their fluid elements have more kinetical energy through most parts of the boundary layer than those of laminar boundary layers. As a result, turbulent boundary layers resist better adverse pressure gradients and maintain the flow attached for much larger distances than laminar boundary layers. This ability to maintain the flow attached for larger distances results in turbulent boundary layers having much less pressure drag than laminar boundary layers.

$$D_p^{laminar} > D_p^{turbulent} \tag{1.26}$$

1.5.4. Flow transition

Similar to flow separation, flow transition is very compelling for flow analysis. The phenomenon of transition consists of the transformation of a laminar boundary layer into a turbulent boundary layer. For an airfoil, the boundary layer usually starts laminar at the leading edge, and at some point downstream, instabilities -caused by the surface roughness, heating of the fluid, adverse pressure gradients, etc.- start to appear, causing a transition to a turbulent boundary layer.

As shown in figure 1.6, flow transition occurs within a finite region in the streamwise direction. Nevertheless, for simplicity in the analysis, the transition region is often modeled as a single point, which depends on many factors related to flow perturbations. For this reason, obtaining the transition point is an interesting problem-specific task for flow analysis.

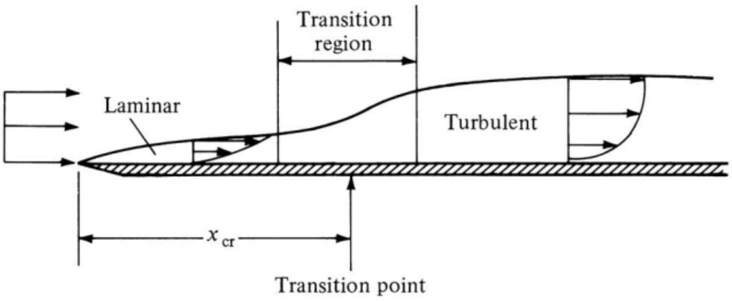

Figure 1.6: Transition process from a laminar to a turbulent boundary layer over a flat plate. x_{cr} stands for the critical location at which the flow can no longer be considered laminar and has to be considered turbulent instead. [13]

CHAPTER 2. NUMERICAL SETUP

In the last chapter, it has been seen how applying statistics to the Navier-Stokes equations leads to the RANS equations and the different turbulence models that close them. Nevertheless, solving the RANS equations is as crucial as formulating them. Unfortunately, just like the Navier-Stokes equations, RANS equations cannot be solved analytically except for highly restricted flows, which in most cases are far from those found in the real world. Fortunately, just like the Navier-Stokes, RANS equations can be solved numerically, thus providing an alternative to empirical observations for studying most real-world flows. For this reason, together with the on-growing computational capacity of the last decades, computational fluid dynamics, famously known as CFD, has become one of the pillars of fluid mechanics, together with theoretical and experimental analysis.

The process for solving the governing equations via CFD, although complex when it comes to the details, is simple to reason. Firstly, the computational domain has to be discretized by means of developing an adequate mesh. Secondly, numerical methods must be applied to solve the corresponding flow equations in each of the mesh nodes. Lastly, once the numerical methods have converged into a solution, the obtained data should be analyzed to draw conclusions about the solved flow behavior. This last stage is what is known as post-processing. In this chapter, the study's implementation of these three stages and the software employed to carry them are presented in detail.

2.1. Definition of the baseline and actuated cases

As stated in the study's introduction, the flow over an SD7003 airfoil in post-stall conditions, concretely $\alpha = 14^\circ$ at $Re = 6 \cdot 10^4$, is studied via RANS simulations. Similarly to the studies made by Tousi et al. [2] [6] and Rodriguez et al. [5] so that later comparisons with their results can be performed easily, the chord length has been taken as C = 1 m, the free-stream velocity as U_∞ = 1 m/s, and the air kinematic viscosity as $\nu = 1/6 \cdot 10^4$ m^2/s. Furthermore, both baseline and actuated cases were solved within a computational domain of dimensions $35C$ x $30C$, which was chosen by taking previous studies conducted by Tousi et al. [2] [6] as a reference.

Figure 2.1 represents the computational domain topology and the different boundary regions. The origin of the cartesian coordinate reference system of the mesh is placed at the leading edge so that its location consists of $(x, y) = (0, 0)$. The inlet is characterized by a semi-circle of a radius $15C$ whose center is located at the leading edge. In addition, both upper and lower boundaries are located at $\pm 15C$. Lastly, the inlet's location can be found at $20C$.

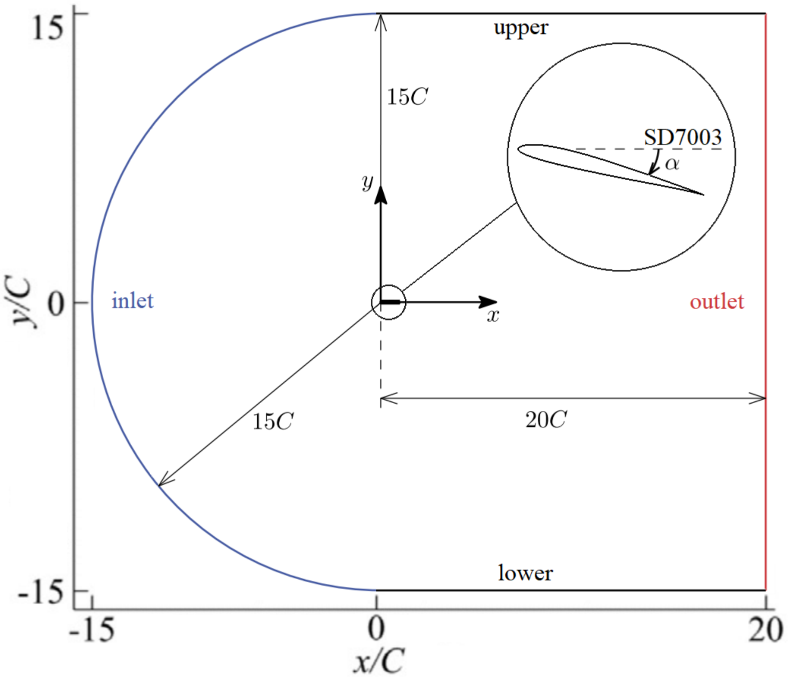

Figure 2.1: Sketch of the computational domain and its different boundary regions, namely inlet (blue line), lower and upper regions (black lines), and outlet (red line).

2.2. Mesh construction

The mesh being ultimately responsible for discretizing the different flow regions where governing equations are solved, its construction makes one of the most sensitive tasks of any CFD problem. Theoretically, the most accurate mesh would be the one whose nodes scales were comparable to the continuum hypothesis scales, as the Navier-Stokes equations are formulated based on this hypothesis. However, such mesh would be unsolvable as the computational time it would require to solve any flow would be completely unfeasible. In contrast, a mesh not fine enough would not be able to capture the flow behavior correctly, thus producing wrong results. For these reasons, a trade-off between accuracy and computational resources must be established.

Achieving such a balance between accuracy and computational resources is not a straightforward task and ends up taking up a high part of the work required to solve a CFD problem. Even though experience and intuition about the flow behavior can play a critical role in reaching an optimal mesh, a convergence study is always required. Therefore, this study being no exception, an optimal mesh in terms of accuracy and computational resources is obtained via a convergence study presented in section 2.5.

As for the software employed for developing the mesh, Gmsh has been used. Gmsh consists of an open-source three-dimensional finite element mesh generator widely used by the CFD community [14]. Together with Gmsh, a hand-made python script has been employed to automatize the development process of both the baseline and actuated meshes. This script, left to the reader's free use in [15], allows the development of a mesh directly by choosing its characterizing parameters, such as the angle of attack, the computational domain dimensions, and the location of the synthetic jet, among others.

2.2.1. Mesh considerations

There exist three main approaches when it comes to discretizing the flow, structured meshing, unstructured meshing, or a hybrid between both. The former discretizes the space using quadrilateral and hexahedral elements for 2D and 3D geometries. In contrast, unstructured meshing relies on triangular and tetrahedral elements for 2D and 3D geometries. Lastly, hybrid meshing takes advantage of both previous approaches by applying them when they are most beneficial to either the results or the computational efficiency of the mesh.

Choosing between the three ultimately relies on the specifics of the problem. Unstructured meshes are often faster to generate than structured ones, as their meshing elements allow algorithms to have more freedom in positioning the mesh nodes. In contrast, structured meshes require cohesion between the different meshing regions, which among other reasons, make its meshing process more complex.

For simple problem geometries, such as airfoils, structured meshes are often more accurate, mainly because they are usually developed by having some kind of knowledge about the presumed flow behavior. However, when it comes to complex geometries where the flow behavior is not so intuitive, the freedom of unstructured meshes may result in more accurate results. As for their computational efficiency, structured meshes require fewer computational resources than unstructured ones due to their memory storing mechanism. As depicted in figure 2.2, structured cells can be easily stored in matrix form due to their very own nature. In contrast, unstructured cells require information about their adjacent nodes and storing positioning, thus requiring more computational capacity.

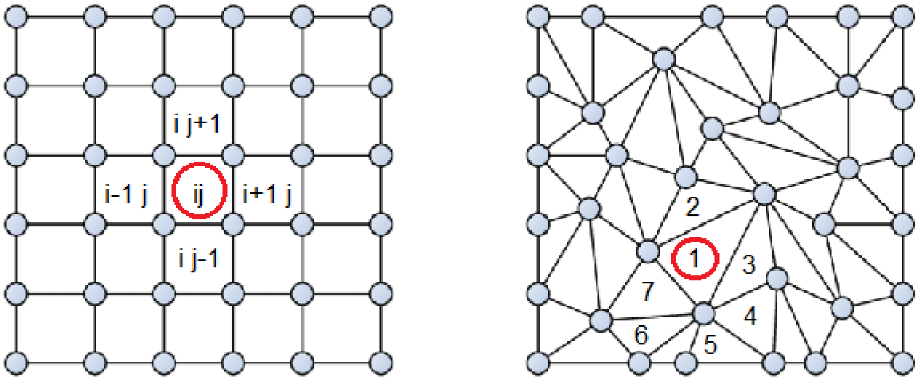

U(i,j) data stored in matrix form

U(i) data stored in vector form containing its direct neighbors

Figure 2.2: Memory storage mechanisms of both structured (left) and unstructured (right) cells.

Once the computational domain has been discretized via one of the previous approaches, the quality of the resulting mesh can be addressed via several parameters. Such parameters are related to the properties of the cells, like orthogonality, homogeneity, skewness, or aspect ratio. Starting with these parameters presentation, orthogonality is of paramount importance to capture properly the gradients of the several flow properties, especially those occurring in the vicinities of a body's surface, as higher densities of cells are often placed there. The concept of orthogonality can be easily understood by looking at the two examples in figure 2.3.

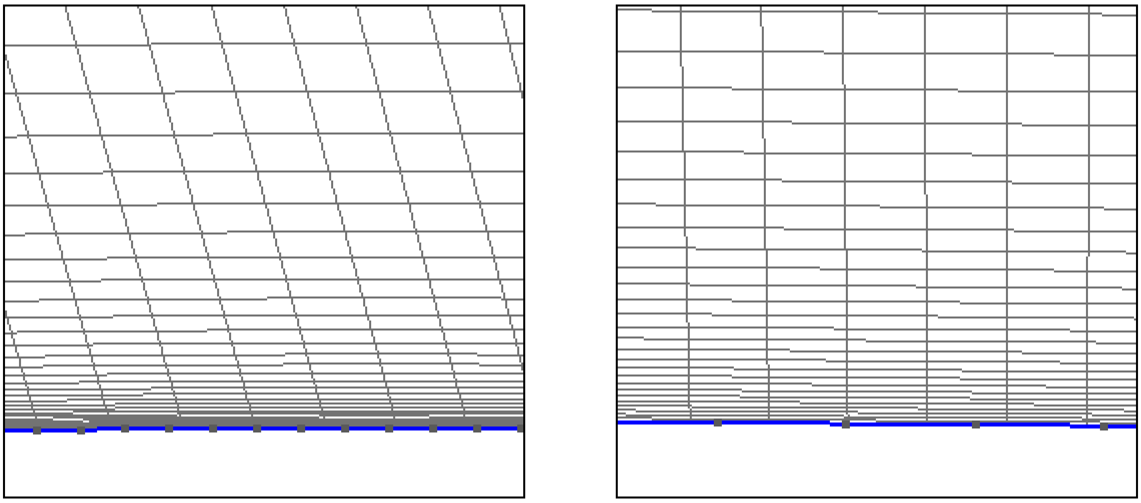
(a) Poor orthogonal region

(b) Rich orthogonal region

Figure 2.3: Different degrees of orthogonality in cells placed in the vicinities of a wall.

In contrast, homogeneity is related to the transition between the different cell density regions. Smooth transitions result in homogeneous cell regions, whereas abrupt transitions lead to high non-homogeneous cell zones. Non-homogeneities make inefficient use of the computational resources as they end up concentrating tons of cells in zones where no such resolution is required. Similar to orthogonality, by looking at figure 2.9, the concept of homogeneity can be easily visualized.

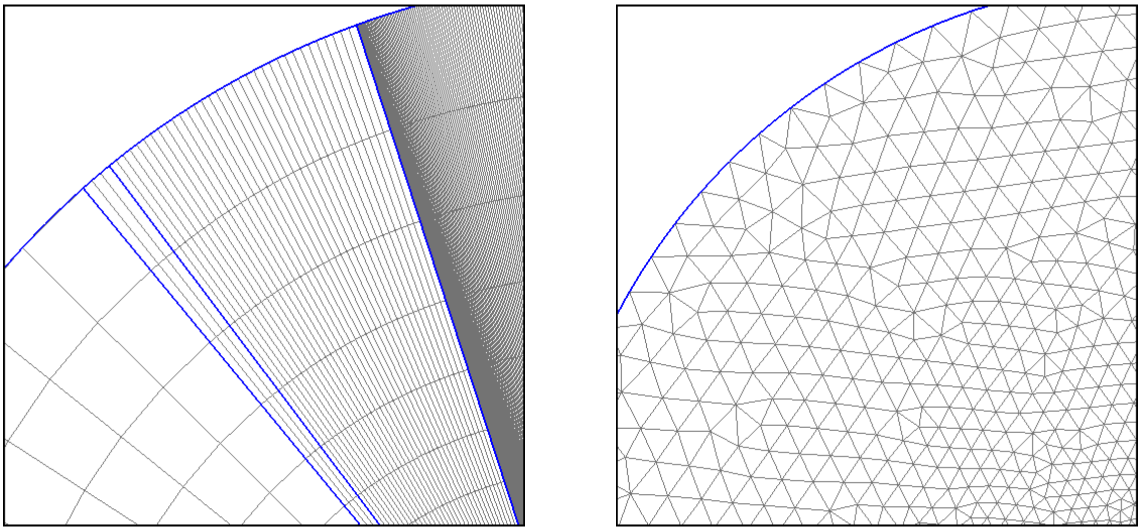
(a) Non-homogeneuous structured cell region

(b) Homogeneous unstructured cell region

Figure 2.4: Different degrees of homogeneity in cell regions located in the vicinities of the inlet.

Additionally, the cell skewness relates the angle θ between two adjacent faces of a cell as pictured in figure 2.5. The ideal value of skewness is 90º, that is the adjacent faces are placed perpendicularly. Contrary, values of skewness smaller than 45º or bigger than 135º worsen notably the quality of the mesh as they produce instabilities and deteriorate the accuracy of the solver. In fact, for complex geometries where these values are unavoidable, some treatment on the flow solver equations is often required.

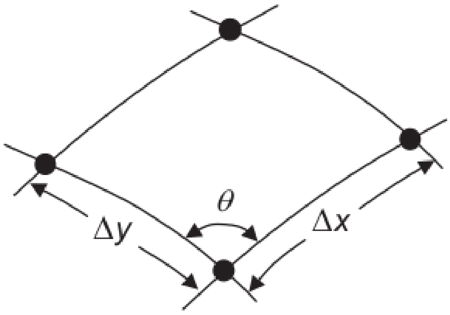

Figure 2.5: Cell skewness of two adjacent cell faces addressed through the angle θ. [16]

To conclude, the aspect ratio evaluates the proportions of two adjacent faces of a cell as the ratio between their respective lengths. The ideal value of aspect ratio is unitary, that is both adjacent faces have the same length. In contrast, large and close to zero values should be avoided whenever possible as they degrade the accuracy of the results and worsen notably the iterative performance of the flow solver, thus resulting in slower simulation convergence. Similar to orthogonality and homogeneity, the concept of aspect ratio can be better comprehended by looking at figure 2.6.

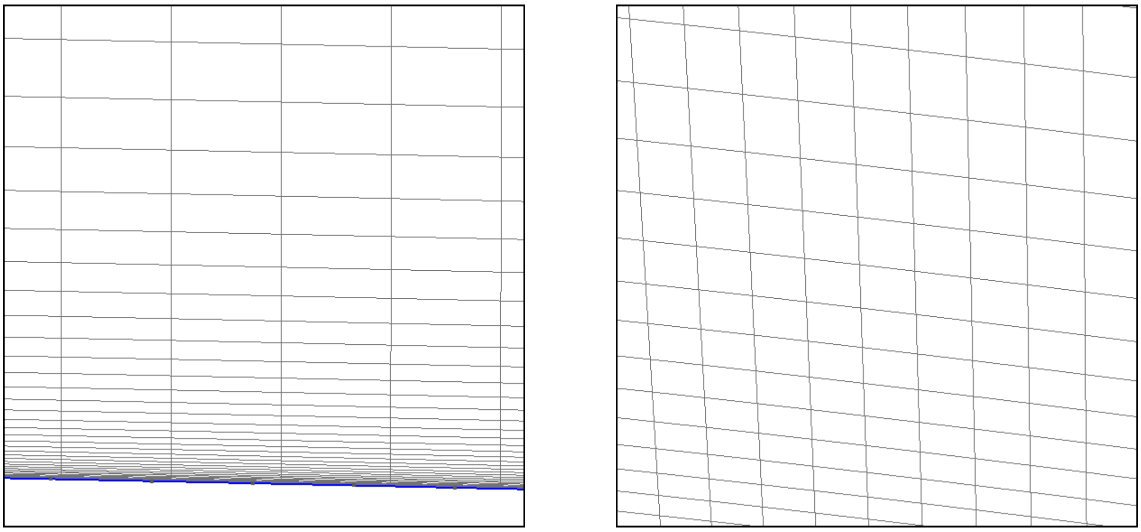

(a) Cells with high values of aspect ratio

(b) Cells with desirable values of aspect ratio

Figure 2.6: Regions of cells containing different values of aspect ratio.

2.2.2. Mesh Approaches

Developing an optimal mesh for the discretization of the computational domain has been one of the major challenges encountered in conducting this study, as finding a good quality mesh whose accuracy and computational requirements were feasible has been a complex and lengthy task. Before reaching a final mesh, three different approaches were taken in its design. The first approach consisted of a purely structured C-type grid with four sections corresponding to the far, mid, near, and closest regions, which are depicted in figure 2.7. These different regions aimed to produce a smooth transition between the low-density cell zones of the far region and the high-density cell zones of the closest region in order to promote cell homogeneity.

Unfortunately, to maintain the number of cells low enough so that the time scales of the simulation remained feasible, this approach led to high non-orthogonalities, several non-homogeneous regions, high values of skewness, and large aspect ratios. As a result, inefficient use of the computational resource was being done as the solver required many iterations between time steps in order to advance further with the simulation.

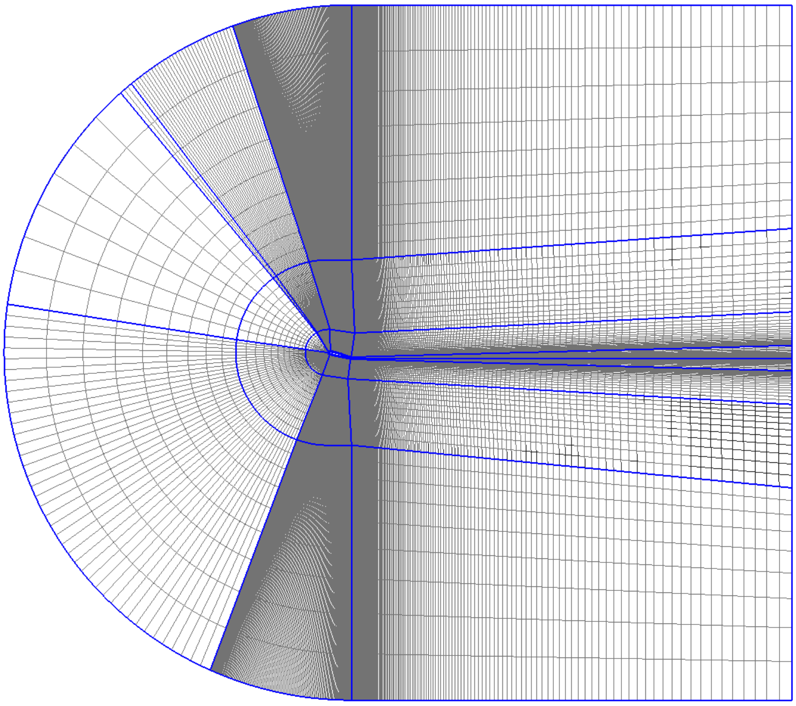

Figure 2.7: Illustration of the first mesh approach. The different mesh regions can be identified as far, mid, near, and closest regions by their respective distance from the inlet to the leading edge.

Aiming of solving most of the downsides of the previous mesh, a second approach consisting of a hybrid mesh between unstructured and structured meshing was taken. This approach replaced the far and mid regions structured cells with unstructured ones so that high values of aspect ratio and non-homogeneities were no longer an issue. In addition, the near and closest regions were refined in order to better capture the wake and the main velocity gradients.

Unfortunately again, as can be seen in figure 2.8, this second approach still maintained some of the previous issues like high aspect ratios and non-homogeneities in the near and closest regions. As a result, the mesh performance towards the flow solver was still not good enough and many computational days were required to reach convergence.

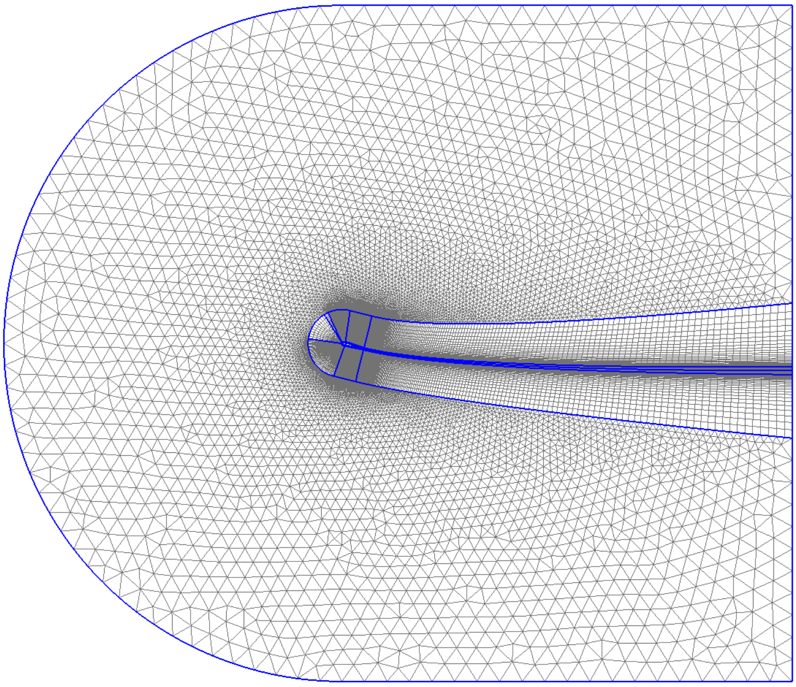

Figure 2.8: Illustration of the second mesh approach. Non-homogeneities can be easily spotted in the near region located in front of the leading edge. Additionally, in the wake closest regions, not only non-homogeneities can be noticed but also high aspect ratios.

Lastly, a third and final approach solved most of the flaws of the previous two. This third mesh replaced the structured cells of the near region with unstructured ones and reduced the wake divisions to a small section in the trailing edge, as pictured in figures 2.9(b). In addition, more meshing partitions were implemented across the airfoil's surface to improve the orthogonality of the cells in the closest region. As a result, this new mesh had homogeneous low-density cell zones in the vicinities of the boundaries of the computational domain, that smoothly transitioned to the high-density cell zones of the closest region. Moreover, to capture properly the possible separation bubbles caused by the airfoil being in such post-stall conditions, a surrounding unstructured region with increased cell resolution was implemented as pictured in figure 2.9(a).

To conclude, in order to make the baseline and actuated cases mesh-independent, the synthetic jet section was introduced into the mesh with the location and width corresponding to the optimal AFC parameters found by Tousi et al. [2] as seen in figure 2.9(c). Nevertheless, in the baseline case, the jet patch takes the same boundary conditions as the upper and lower airfoil surfaces, thus treating the jet as part of the upper wall.

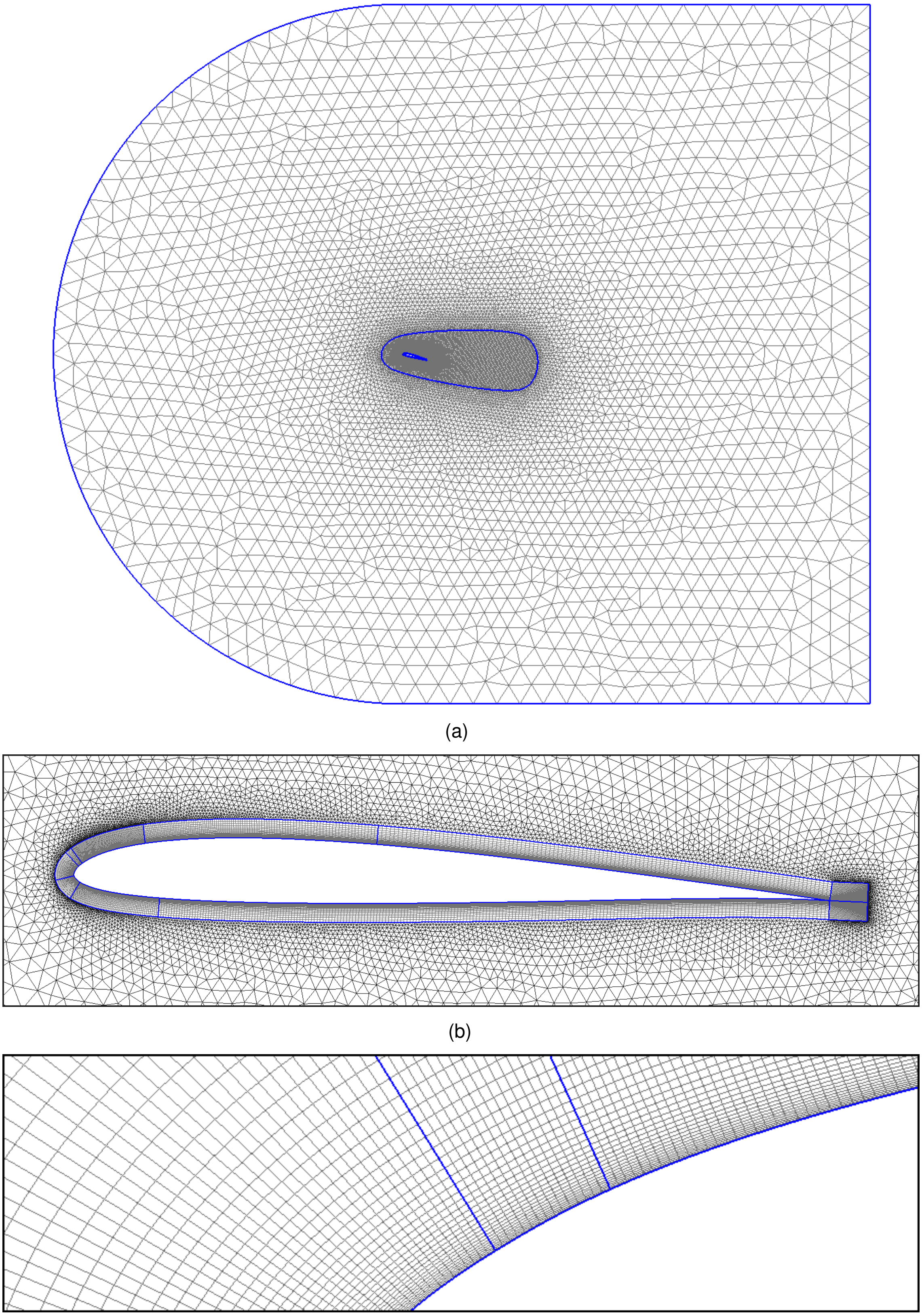

(a)

(b)

(c)

Figure 2.9: (a) Illustration of the final mesh approach depicting the surrounding unstructured regions and its smooth transition of the cell resolution from the outer zones to the vicinities of the airfoil. (b) Close view of the closest region and the trailing edge section. (c) Close view of the closest region and its implementation of the synthetic jet section.

2.3. Flow solution

As mentioned in the chapter's introduction, once a proper discretization of the computational domain has been obtained, the following natural step is to solve the governing equations over the different mesh nodes. The software employed during the study to perform this task has been OpenFOAM, which consists of an open-source continuum mechanics problem solver most known for its CFD applications. OpenFOAM's extreme flexibility for setting up flow conditions and resolution methods has made it one of the preferred CFD software for researchers. Moreover, thanks to its spread use and actively developing community, which constantly has been upgrading the software since its first release in 2004, OpenFOAM counts with vast reliable setups for different flow scenarios across many engineering fields.

2.3.1. Flow solver

One of the most crucial tasks to be done in order to solve a CFD problem with OpenFOAM is choosing an adequate solver among its wide offer. When it comes to incompressible turbulent flows, OpenFOAM counts with several solvers [17] that provide numerous useful features for the different types of flow problems within this context. Among all of them, the two solvers that have been found most adequate for the study's context, incompressible turbulent flow over an airfoil, are the following:

- SimpleFoam, a steady-state solver for incompressible turbulent flows.
- PisoFoam, a transient solver for incompressible turbulent flows.

Between the two, the solver chosen for this numerical setup has been PisoFoam. The reason behind this decision is its capability to handle transient behaviors, which as actuation via synthetic jets is intended, it allows analyzing the flow behavior across the several stages of the membrane oscillation.

2.3.2. Boundary conditions

Similar to developing an optimal mesh or choosing an adequate solver, defining an appropriate set of boundary conditions is of paramount importance to produce meaningful results. Being boundary conditions the ultimately responsible for correctly representing the flow subjected to study, imposing inadequate values would imply solving a different flow than the one intended, thus wasting computational and human resources.

Before proceeding further with the formulation of the different boundary conditions for the three turbulence models, a simple yet important concept worth mentioning is the difference between Neumann and Dirichlet boundary conditions. A Neumann or second-type boundary condition takes place over the derivative of the variable being imposed on the physical boundary. In the case of OpenFOAM's nomenclature, a common Neumann boundary condition is 'zeroGradient'. In contrast, Dirichlet or first-type boundary conditions specify the value directly over the variable itself being imposed on the physical boundary.

Regarding the boundary conditions for both upper and lower computational domain edges, they retain the same conditions for all three turbulence models. As the flow in these regions is supposed to move tangentially to them $\vec{V}_{up/low} = (U_\infty, 0, 0)$ an OpenFOAM's 'symmetryPlane' boundary condition is applied for all fluid variables.

In a similar manner, both p and velocity U conditions remain the same for each of the three turbulence models. For these two parameters, common boundary conditions found in the literature have been applied. At the inlet, the uniform velocity field takes the value of $\vec{V} = (U_\infty 0, 0)$ along with a 'zeroGradient' Neumann boundary condition for the pressure field. At the outlet, the roles are reversed, and a Dirichlet boundary condition is imposed over the pressure field $p = 0$, whereas a 'zeroGradient' Neumann boundary condition over the velocity field. Lastly, the airfoil surface is treated as an impermeable no-slip wall by imposing a Dirichlet boundary condition on the velocity field $\vec{V}_{wall} = (0, 0, 0)$ and a 'zeroGradient' Neumann boundary condition on the pressure field.

Lastly, the synthetic jet patch is initially treated as a wall, just like the upper and lower airfoil surfaces in the baseline case, thus having the very same boundary conditions. In contrast, when actuation is performed, it takes the corresponding boundary conditions of such a specific actuation configuration. No further detail about these last boundary conditions will be given in this section but in sections 3.2.2. and 3.2.3. instead so that it becomes easier to follow the thread of this chapter.

2.3.2.1. $Realizable - k - \varepsilon$ *and* $SST - k - \omega$ *boundary conditions*

The $realizable - k - \varepsilon$ and $SST - k - \omega$ models share the same boundary conditions for all flow properties except for their distinctive second transport variables, namely ε and ω. Taking the study conducted by Catalano and Tognaccini [3] as a reference, the free-stream ratio between the turbulent viscosity ν_t and the air kinematic viscosity ν is set as $\nu_T/\nu = 10^{-9}$, thus leading to a turbulent viscosity of $\nu_t = 1.667 \cdot 10^{-14}\ m^2/s$ in the free-stream. In the same manner, the turbulent intensity has been settled at $I = 10^{-6}$, which according to the guidelines of the model in OpenFOAM's documentation [18] leads to a free-stream turbulent kinetic energy of $k = 1.5 \cdot 10^{-12}\ J/kg$. Moreover, ε and ω at the free-stream have been obtained according to the expressions found in their corresponding model's documentation [18] [19], as $\varepsilon = 3.019 \cdot 10^{-19}\ J/(kg \cdot s)$ and $\omega = 2.236 \cdot 10^{-6}\ 1/s$. Lastly, wall functions have been applied on the jet, upper, and lower surfaces.

Table 2.1: $Realizable - k - \varepsilon$ boundary conditions.

Flow variable	Inlet	Outlet	Airfoil
$\vec{V}$	(U_∞, 0, 0)	zeroGradient	(0, 0, 0)
p	zeroGradient	0	zeroGradient
ν_t	1.667E-14	0	nutLowReWallFunction
k	1.5E-12	zeroGradient	kLowReWallFunction
ε	3.019E-19	zeroGradient	epsilonWallFunction

Table 2.2: $SST - k - \omega$ boundary conditions.

Flow variable	Inlet	Outlet	Airfoil
$\vec{V}$	(U_∞, 0, 0)	zeroGradient	(0, 0, 0)
p	zeroGradient	0	zeroGradient
ν_t	1.667E-14	0	nutLowReWallFunction
k	1.5E-12	zeroGradient	kLowReWallFunction
ω	2.236E-06	zeroGradient	omegaWallFunction

2.3.2.2. Spalart-Allmaras boundary conditions

Regarding the boundary conditions for the Spalart-Allmaras model, the free-stream turbulent viscosity is imposed to be equal to the air kinematic viscosity $\nu_t = \nu = 1.667 \cdot 10^{-5}$ m^2/s. As for the modified turbulent viscosity or Spalart-Allmaras variable, following the advice given by Spalart and Allmaras in their original article [11] stating that its value should be zero at the walls and less or equal than half the value of the air kinematic viscosity $\tilde{\nu} \leq \nu/2$ at the freestream, the modified turbulent viscosity is taken as a third of the air kinematic viscosity $\tilde{\nu} = \nu/3 = 5.556 \cdot 10^{-6}$ m^2/s in the free-stream and zero at the walls.

Table 2.3: Spalart-Allmaras boundary conditions.

Flow variable	Inlet	Outlet	Airfoil
$\vec{V}$	(U_∞, 0, 0)	zeroGradient	(0, 0, 0)
p	zeroGradient	0	zeroGradient
ν_t	1.667E-05	0	nutLowReWallFunction
$\tilde{\nu}$	5.556E-06	zeroGradient	0

2.4. Post-processing engine

Concerning the software employed for the post-processing, ParaView and hand-made python scripts have been used to visualize and analyze the results. Paraview consists of an open-source software for data analysis and flow visualization whose development has been oriented toward the scientific community [20]. In fact, its ability to handle large sets of data has favored its usage in many high-level research disciplines. Therefore, it is not surprising that ParaView contains many interesting features for analyzing the results obtained from the simulations. In this manner, it has been used to visualize the flow property fields, extract data about the pressure and skin friction coefficients, and generate frames from each time-step iteration to export the simulation into video format, among others.

Additionally, for tasks that required extracting data from files like comparing graphics, python scripts have been developed to easily conduct them. In addition, it is worth mentioning that the usage of python for developing the several scripts used across this study is due to the author's familiarity with the language, and other languages such as C# or MATLAB could also be used for the same purposes.

Lastly, OpenFOAM's own post-processing tools have also been used to analyze the results. Once the velocity, the pressure, and the different turbulence model variables have been computed, OpenFOAM counts with functions [21] that allow calculating several properties such as aerodynamic force coefficients, values of y^+, the wall shear stress distribution across the airfoil's surface, etc. Moreover, arguably not a post-processing tool, it also counts with a pretty useful 'checkMesh' command that gives information about the mesh quality parameters previously introduced in section 2.2.1.

2.5. Convergence studies

To conclude with the numerical setup, convergence studies of both mesh cell resolution and time-step have been conducted using the Spalart-Allmaras model. The main goal of these studies was to find cell resolutions and time-step values that offered the best compromise between accuracy and computational cost.

Together with the rest of the simulations made during this study, both convergence studies simulations were performed using OpenFOAM's parallel computing environment, which is detailed in OpenFOAM's documentation [22]. Briefly, it consists in decomposing the mesh and associated flow fields, so each processor of the CPU solves one of these partitions. In this case, the mesh was decomposed into four partitions, each of which was solved using an Intel(R) Core(TM) i7-7700HQ @ 2.80GHz CPU processor.

2.5.1. Mesh convergence study

The mesh convergence study tested four different cell resolutions (A, B, C, and D) over the final mesh approach presented in section 2.2.2. to address their performances in terms of both computational cost and accuracy of the results. In addition, as the time-step convergence study was still to be performed, a low enough time step of $\Delta t = 4 \cdot 10^{-5}$ s was used to ensure the results were reliable.

Table 2.4: Time-averaged aerodynamic performance parameters and mesh characteristics for the four different cases.

Mesh	N_{cells}	y^+	X_s/C	C_l	C_d	η	$t_{convergence}$
A	30634	0.827	0.016	0.817	0.201	4.06	6h 34min
B	52468	0.827	0.015	0.813	0.201	4.04	11h 33min
C	76186	0.358	0.015	0.814	0.201	4.05	21h 56min
D	122536	0.207	0.015	0.814	0.201	4.05	42h 16min

Table 2.4 depicts the main characteristics of the four different meshes tested. The second of its columns displays the total number of cells within the computational domain, ranging from 30634 for the coarsest mesh to 122536 for the finest one. The third column exposes the maximum y^+ value reached until simulation convergence. The fourth column presents the separation point where the flow detaches, obtained as the location where the skin friction coefficient became negative. The following three columns depict the airfoil's lift,

drag, and aerodynamic efficiency coefficients. Lastly, the last column displays the time required for the solver to obtain a converged solution of up to 5 decimals.

The minute discrepancies between the different mesh resolutions show that the work carried out during the different meshing approaches paid off, as the aerodynamic performance coefficients of all four mesh resolutions are well within the scope of those found in the literature. Nevertheless, as these coefficients are obtained via integrating the corresponding flow properties across the airfoil's surface, a cancellation between their errors can lead to these numerical values being misleading about the flow behavior. For this reason, analyzing local quantities such as the pressure or skin friction distribution across the chord is a better option for analyzing the flow dynamics.

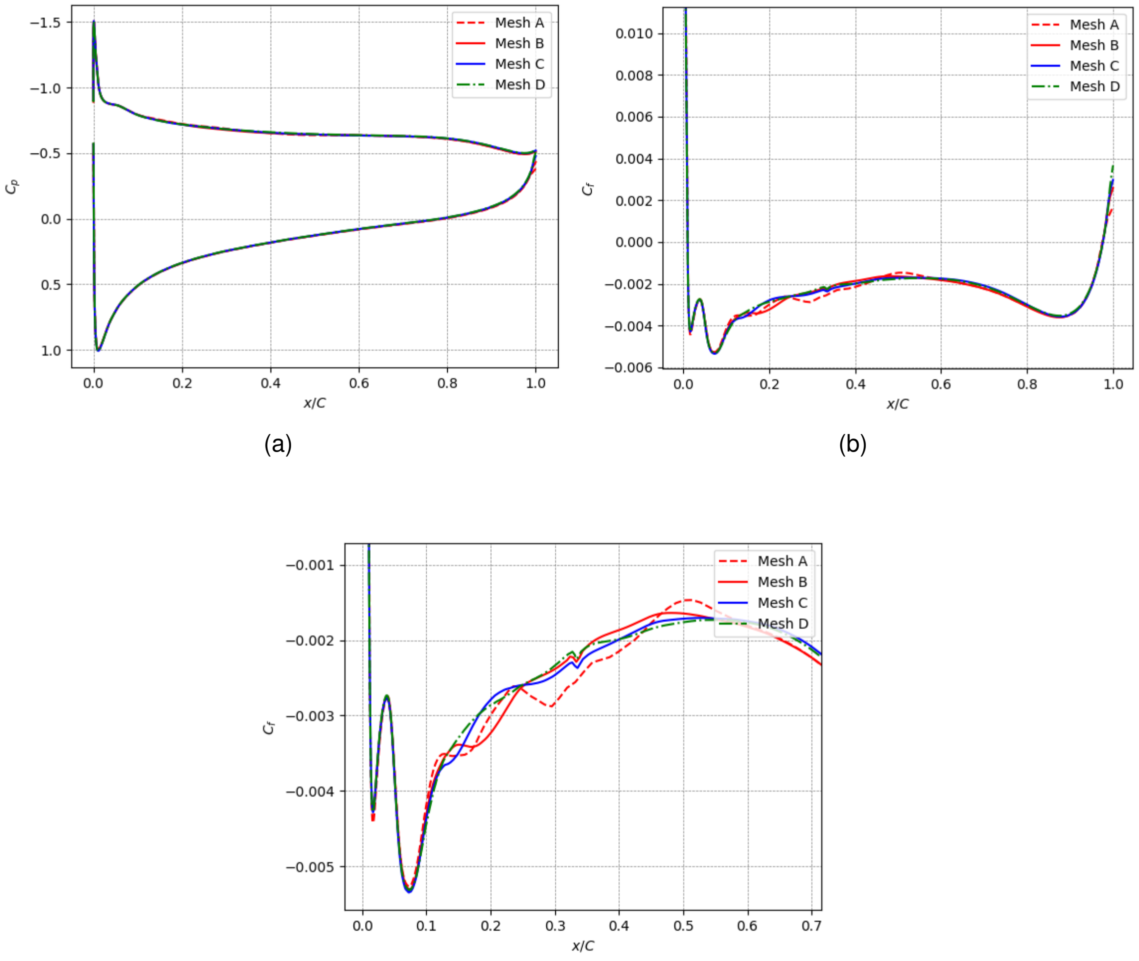

(a)

(b)

(c)

Figure 2.10: Mesh convergence study (a) pressure $C_p(x/C)$ and (b) skin friction $C_f(x/C)$ coefficient distributions and (c) a closer view of the skin friction coefficient distribution over the first half of the chord.

The pressure and skin friction coefficient distributions depicted in figures 2.10(a) and 2.10(b) show a nice agreement between the results obtained by the four meshes, especially for pressure. Nevertheless, a region right before the middle chord in the skin friction coefficient distribution seems to be solved differently for the four mesh resolutions. A closer view of this region shown in figure 2.10(c) reveals a tendency towards an increasing oscillatory behavior in the skin friction coefficient as the mesh cell resolution is reduced. As expected, the cell resolution that best matches the skin friction coefficient distribution of the finest mesh corresponds to mesh C, which contains the second-highest number of cells.

On the whole, meshes B, C, and D present pretty similar results despite having notoriously different cell resolutions and convergence times. Nevertheless, to decide which mesh represents the best balance between accuracy and computational cost, the specifics of the study have to be taken into account. Regarding the accuracy of their results, meshes B and C give almost identical results despite B having 31% fewer cells than C. Nonetheless, B's value of y^+ is 2.31 times higher than C's, which despite proving to be low enough for the baseline case, it might end up deteriorating the results when actuation is performed and larger gradients appear near the airfoil's surface. As for the computational cost, mesh D takes more than a day and a half to reach convergence, while mesh C only takes half that time while providing the same aerodynamic force coefficient values and almost identical pressure and skin friction distributions. In light of this, as the study working period is relatively short, counting with double the computational resources at the expense of losing a minute degree of accuracy, not only would make the errors in the simulations less prohibitive but also would allow conducting more simulations. As a result, the mesh resolution that proves more optimal in terms of accuracy and computational cost corresponds to mesh C.

2.5.2. Time step convergence study

Similarly to the mesh quality, which can introduce errors in the results and make the solver unstable, the time step also affects the accuracy and stability of the flow solver. Large time steps fail to capture properly the flow's behavior since they exceed some of the flow phenomenon timescales. For this reason, time steps must fulfill the Courant–Friedrichs–Lewy condition, commonly known as CFL. This condition states that the distance the information of one cell travels in one time-step must be lower than the distance between mesh elements, which is to say, the cell information is only propagated to their direct neighbors. Mathematically, this condition is formulated by imposing the Courant number to be smaller or equal to unity, which results in the following expression:

$$C = \Delta t \left(\sum_{i=1}^{n} \frac{u_{x_i}}{\Delta x_i} \right) \leq 1 \tag{2.1}$$

where u_{x_i} is the magnitude of the i component of the velocity, Δx_i the i projection of the distance between two neighbor mesh nodes, and n denotes the flow's dimension, that is $n = 2$ for two-dimensional flows and $n = 3$ for three-dimensional flows. From both its physical and mathematical interpretations, it can be seen that the finer the mesh is, the smaller the time-step must be. For this reason, to perform this convergence study, four different time steps of $2 \cdot 10^{-5} s$, $4 \cdot 10^{-5} s$, $6 \cdot 10^{-5} s$, and $8 \cdot 10^{-5} s$ that properly resolve the flow and fulfill the CFL condition have been chosen.

Table 2.5: Time-averaged aerodynamic performance parameters, required time to reach convergence, and maximum Courant number reached on the converged solution for the four different cases.

Δt	C_l	C_d	η	$t_{convergence}$	C_{max}
$2\cdot10^{-5}\ s$	0.814	0.201	4.05	41h 19min	0.1022
$4\cdot10^{-5}\ s$	0.814	0.201	4.05	21h 56min	0.2045
$6\cdot10^{-5}\ s$	0.813	0.201	4.04	15h 12min	0.3068
$8\cdot10^{-5}\ s$	0.813	0.201	4.04	10h 29min	0.4091

Depicted in table 2.5, the results of the convergence study show a stunning agreement between the four-time steps. It should be encouraging as it proves that the chosen time steps properly resolve the flow. In fact, the maximum Courant number obtained once convergence is reached is still far below one, $C^{max}(8\cdot10^{-5}) = 0.4091$, meaning that most likely the time step could still be increased further without leading to any stability issues. Regarding the aerodynamic performance coefficients slightest to no discrepancies can be spotted between the four cases, reaching a maximum error of ε_η = 0.25% between the smallest and largest time step for the aerodynamic efficiency. Nevertheless, as seen in the mesh convergence study, an analysis of local quantities like the pressure or skin friction coefficient distributions is required to ensure such concordances.

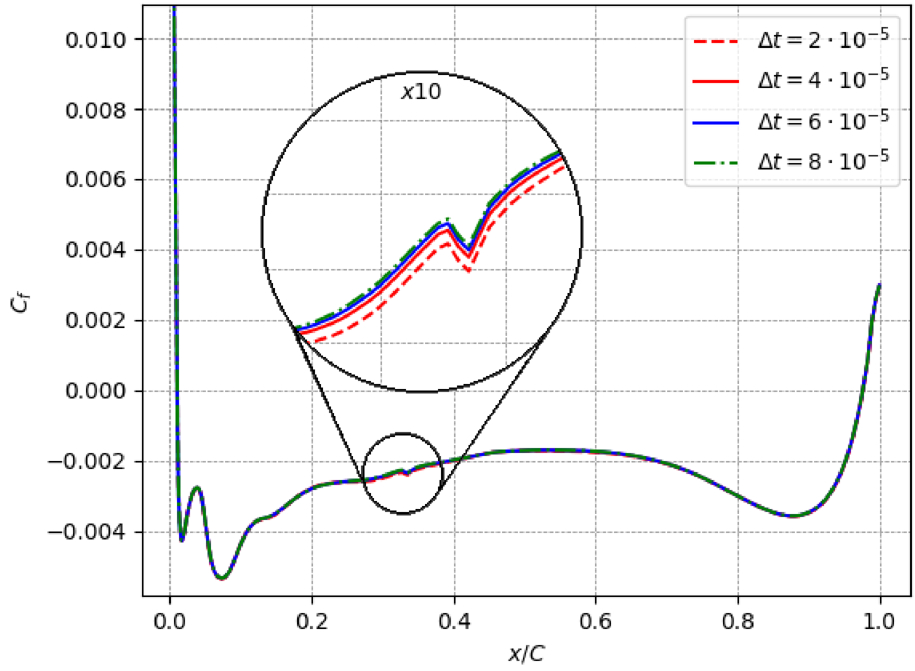

Figure 2.11: Time step convergence study skin friction coefficient $C_f(x/C)$ distributions with a x10 zommed section at $x/C = 0.3$

Both pressure and skin friction coefficients show identical distributions among the four-time steps, especially for pressure, whose distributions were literally on top of each other. As for the skin friction coefficient, only a minute difference in the four distributions can be spotted in the first third of the chord. Portrayed in figure 2.11, there seems to be a different trend in the calculated skin friction between the four cases in this region. However, this difference is so minuscule, in the order of 10^{-4}, that can be neglected for all purposes.

In light of these findings, as accuracy seems to be unaffected, picking the time-step that requires less computational resources to reach convergence, namely $8 \cdot 10^{-5} s$, should be the wisest choice. However, as actuation alters the velocity field with respect to the baseline case, and taking the values employed by several studies available in the literature as a reference [2] [3] [6], the author opted to be cautious and selected a time step of $4 \cdot 10^{-5} s$ to conduct the rest of the simulations.

CHAPTER 3. RESULTS

In this chapter, the obtained results from the baseline and actuated cases are presented, analyzed, and compared with the available literature. This later comparison of the results with those available in the literature is essential to ensure their physical meaningfulness. For this purpose, three numerical studies, which are described briefly in this introductory paragraph, have been considered. The former, carried out by Tousi et al. [2], applied genetic algorithms for AFC optimization across pre-stall and post-stall angles of attack on an SD7003 airfoil at $Re = 6 \cdot 10^4$ using the Spalart-Allmaras model, which concluded that as the angle of attack increases, the benefits of AFC become more pronounced. The second, carried out by Rodriguez et al. [5], focused on the effects of actuation mechanisms on the boundary layer of an SD7003 airfoil at $Re = 6 \cdot 10^4$ via 3D-LES. The latter, also conducted by Tousi et al. [6], employed their previously optimized parameters obtained in [2] to assess the aerodynamic performance of an SD7003 airfoil within the same context but via 3D-LES instead of RANS.

3.1. Baseline case

The resolution of the baseline case via the different turbulence models provided the first discovery of the study. Unfortunately, both turbulent-kinetic-energy models, namely $realizable-k-\varepsilon$ and $SST-k-\omega$ failed to solve the flow in such post-stall conditions. Presented in figure 3.1, the time evolution of the lift coefficient of both models reveals an erratic oscillatory behavior that neither shows any sign of reaching convergence nor a periodical mode despite being simulated for over 100-time units. Moreover, such behaviors are also located far away from the values obtained by the literature, thus proving that these models are not capable of solving the flow properly in such post-stall conditions.

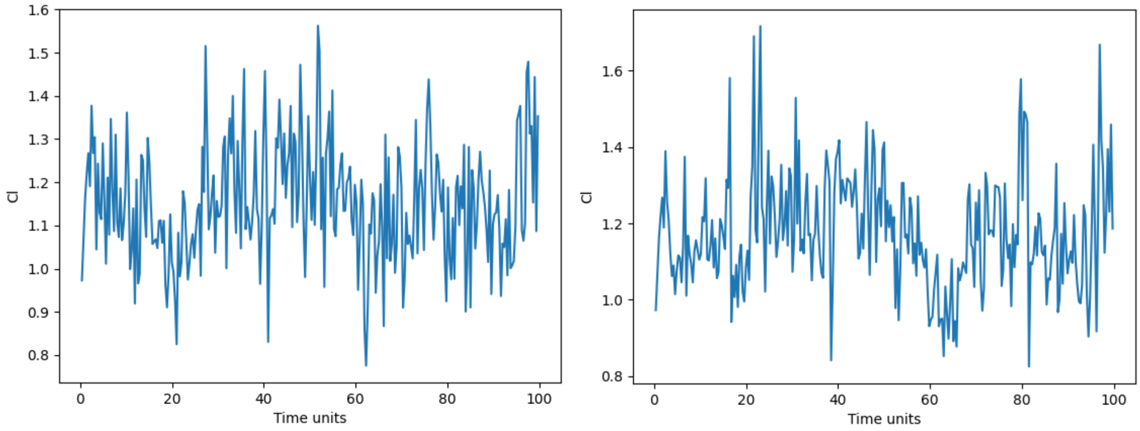

(a) (b)

Figure 3.1: Time evolution of the lift coefficient obtained with the (a) $realizable-k-\varepsilon$ and (b) $SST-k-\omega$ models.

In contrast, the lift coefficient obtained with the Spalart-Allmaras model reaches convergence smoothly after an initial transient regime of 25-time units characterized by a decreasing oscillation towards 0.814 as portrayed in figure 3.2. As will be seen when performing the comparison with the literature, this value of the lift coefficient is well within the range of the values found in the literature. It is important to mention that these behaviors are not, in any case, exclusive of the lift coefficient, as the drag coefficient and other fluid variables like the velocity or pressure fields behave in the same way.

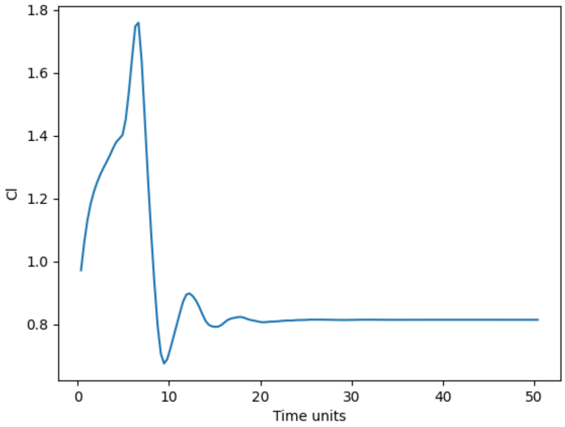

Figure 3.2: Time evolution of the lift coefficient obtained with the Spalart-Allmaras model.

Regarding the results of the $realizable - k - \varepsilon$ and $SST - k - \omega$ models, the author proposes two hypotheses to explain such erratic behaviors. The first hypothesis is that as the convergence studies of both the mesh and timestep have been conducted with the Spalart-Allmaras model, it might be possible that in order to converge, both $realizable - k - \varepsilon$ and $SST - k - \omega$ models require a finer mesh or/and timestep. Nevertheless, this seems unlikely as the CFL condition is fulfilled during the simulations and the OpenFOAM wall functions employed for the three turbulence models require the mesh to have similar y^+ values.

The second hypothesis is that the $realizable - k - \varepsilon$ and $SST - k - \omega$ models fail to accurately solve the flow simply because of their own nature. As seen in section 1.4., turbulence models are built upon flow assumptions, which in some circumstances end up falling short of representing reality. The standard $k - \varepsilon$ model, for example, is intended for fully developed turbulent flows, which clearly is not the context of the baseline case. This hypothesis is backed up by the lack of available literature on SD7003 airfoils in post-stall conditions using any type of turbulent-kinetic energy model. In fact, a study conducted by Catalano and Tognaccini [3] where a modification of the $SST - k - \omega$ model was employed to study an SD7003 airfoil at pre-stall conditions, concretely at $\alpha \in [4^\circ, 12^\circ]$, stated that as the angle of attack increases, the choice of the turbulence model itself results crucial.

The baseline case results obtained via the Spalart-Allmaras model show interesting flow phenomena. Pictured in figure 3.3, the velocity streamlines reveal a large recirculating region that covers the vast entirety of the chord together with a smaller one on the trailing edge. In light of such a big recirculating region, it is safe to say that the flow separates early in the airfoil's upper surface. Furthermore, since low values of turbulent viscosity are encountered near the airfoil's upper surface across the entire chord, especially in the leading edge vicinities, it can be deduced that the boundary layer is still laminar when separation occurs.

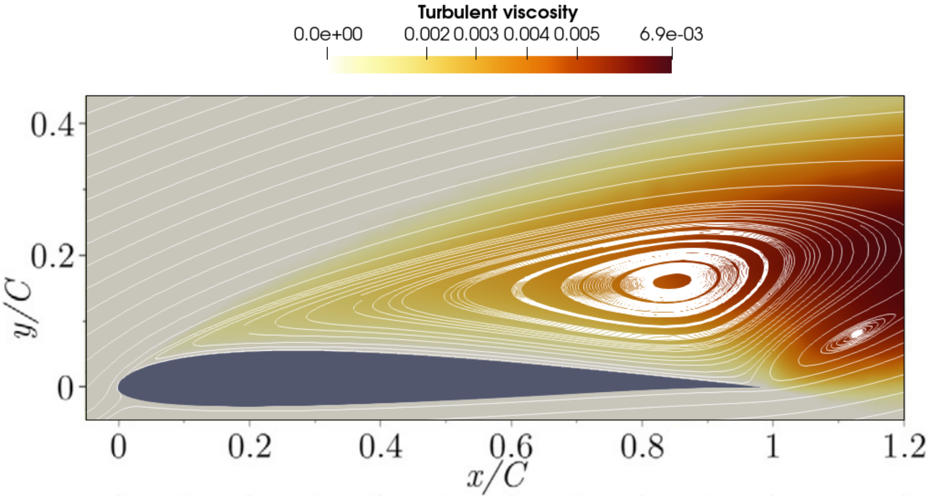

Figure 3.3: Velocity field streamlines and turbulent viscosity contours of the baseline case obtained with the Spalart-Allmaras model.

To conclude whether the boundary layer is still laminar or not when separation occurs, its velocity profiles across five different locations in the leading edge vicinities are presented in figure 3.4. From 3.4(a) it can be concluded that separation does in fact occur in the very early chord, concretely at $x/C = 0.015$, as the wall-normal velocity gradient cancels in the surface's vicinities in this chord location. As for the type of boundary layer, a closer view of these profiles displayed in figure 3.4(b) shows that before the flow starts being reversed, its velocity profile (red dashed line) corresponds to the one of a laminar boundary layer introduced in section 1.5.3.

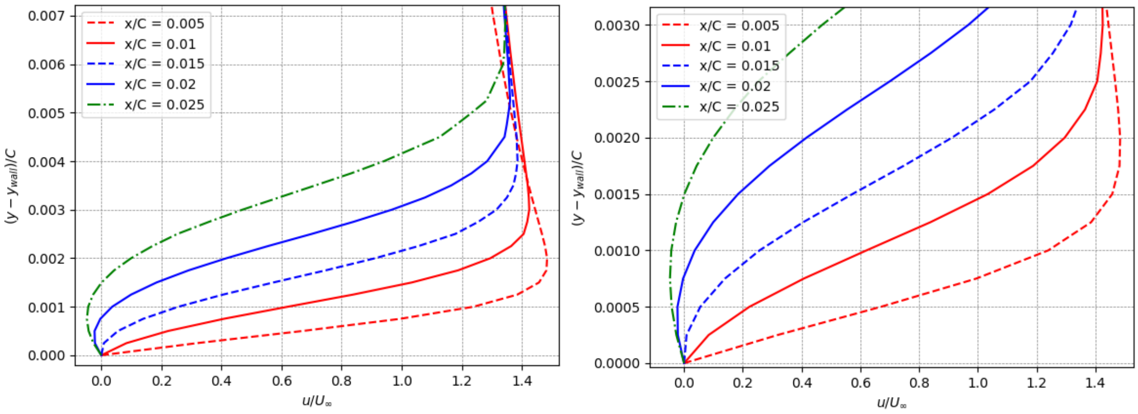

(a)

(b)

Figure 3.4: Evolution of the upper-surface boundary layer velocity profile in the vicinities of the leading edge obtained with the Spalart-Allmaras model.

Regarding the comparison of the results with the literature, as the $realizable - k - \varepsilon$ and $SST - k - \omega$ models were not capable of solving the flow, only the Spalart-Allmaras results are considered. To perform this task several parameters regarding the airfoil's aerodynamic performance and flow variables, like the pressure or skin friction coefficient distributions, are employed.

Table 3.1: Time-averaged aerodynamic performance coefficients of the baseline case and their respective errors with respect to the values found in the literature.

Studies	C_l	ε_{C_l}	C_d	ε_{C_d}	η	ε_η
Present - SA	0.814	-	0.201	-	4.05	-
Tousi et al. - SA	0.798	+2.00%	0.204	-1.47%	3.91	+3.58%
Rodriguez et al. - LES	0.886	-8.12%	0.238	-15.55%	3.72	+8.87%
Tousi et al. - LES	0.895	-9.05%	0.239	-15.89%	3.74	+8.29%

Depicted in table 3.1, the aerodynamic performance parameters show a close agreement with the results obtained by Tousi et al. [2], not exceeding an error of $\varepsilon^{max} = 2\%$ neither in the lift nor the drag coefficients. Nonetheless, due to error propagation, the aerodynamic efficiency has a slightly bigger error than those of the lift and drag coefficients. This agreement with the results obtained by Tousi et al. [2], which also employed the Spalart-Allmaras model in their study, shows that despite using different numerical setups, both lead to similar solutions, thus proving its reliability.

In contrast, when compared to LES results, the level of error notably increases in all three performance parameters. The results presented here results clearly underestimate aerodynamic force coefficients, especially the drag, leading to a maximum error of up to $\varepsilon^{max}_{C_d} = -15.89\%$ with respect to the value found by Tousi et al. in their latest study [6]. This phenomenon exposes some of the flaws in the RANS approach for solving such a separated flow. It is worth remembering that RANS models are at the bottom of the scale in terms of accuracy, followed by LES and ultimately by DNS. As a result, it is not surprising that RANS results fall short in terms of accuracy when they are compared to those of LES.

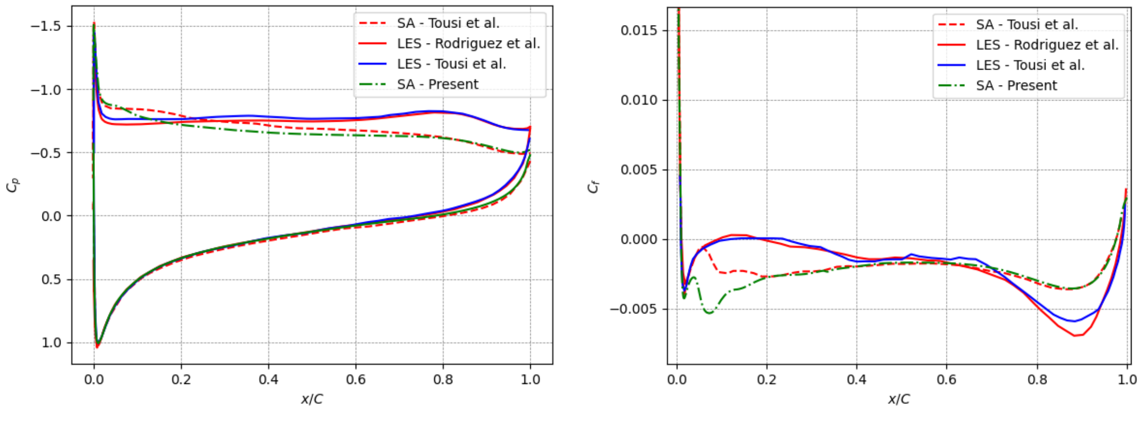

(a)

(b)

Figure 3.5: Baseline case (a) pressure $C_p(x/C)$ and (b) skin friction $C_f(x/C)$ coefficient distributions comparison with the literature.

Nonetheless, as previously mentioned in section 2.5.1., basing the validation of the results only on the aerodynamic force coefficients can be misleading and lead to wrong conclusions. Aggregate quantities like the lift or drag coefficients are derived from a sum of local quantities across the airfoil's surface. For this reason, they can find themselves compensated by the several values across the chord, and even though their values can be well within the scope of literature, the flow dynamics behind them can be quite different than those from the literature. Therefore, analyzing local quantities such as the pressure or skin friction coefficient distributions gives a more insightful look into the flow dynamics captured by the simulation.

Displayed in figure 3.5(a), the lower surface's pressure coefficient distribution shows a fine agreement with those of the literature except in the last section of the chord where LES results reach lower pressure values than the ones obtained by RANS. In contrast, on the upper surface, several dissimilarities can be spotted across the entire chord. Despite all four distributions having similar suction peaks, LES results present higher decelerations of the flow, which seem to be beneficial for maintaining the overall airfoil's suction, as they achieve higher values across the middle and later chord than RANS. On the other hand, the study's results show a fair agreement with literature RANS results, especially in the trailing edge. After decelerating the flow similarly in the vicinities of the suction peak, SA RANS results obtained by Tousi et al. [2] maintain higher suctions across the middle chord to later on matching again in the trailing edge vicinities. Lastly, this comparison between the four distributions discloses that the higher suctions across the middle and later chord of LES results are ultimately responsible for their higher lift coefficients.

In a similar manner, Figure 3.5(b) displays the skin friction coefficient distribution along the airfoil's upper surface. Again, all four studies obtain identical distributions in the vicinities of the leading edge, thus leading to similar values of the separation point. Nevertheless, clear differences between RANS and LES results start to appear after separation. Both LES results present pretty similar values of the skin friction coefficient across the entire chord except for a small region in the vicinities of the trailing edge. In contrast, despite both RANS results presenting identical distributions of the skin friction coefficient in the vast majority of the airfoil's upper surface, they differ notably in the first part of the chord, where the distribution obtained by Tousi et al. [2] reaches a better agreement with those of LES results. In addition, a crucial difference between RANS and LES results that might explain why RANS drag coefficients differ so much from those of LES can be found in this region. LES studies reach positive values for the skin friction coefficient indicating that the flow reattaches. Even though Tousi et al. RANS results reach values close to zero, neither the study's implementation of the Spalart-Allmaras model nor the one of Tousi et al. is capable of predicting reattachment, thus depicting some of the RANS limitations regarding flows in such post-stall conditions.

3.2. Actuated cases

Once the integrity of the numerical setup has been assessed by comparing the baseline results with those from the literature, a further study focused on Active Flow Control via Synthetic Jet Actuators (AFC-SJA) has been carried out. This AFC study can be decomposed into two main parts. The first one evaluates the performance of the optimum SJA parameters found by Tousi et al. [2] in order to address the study's numerical setup reliability for the actuated cases. The second part, in contrast, takes a different approach by studying the effects of an SJA tangential configuration on the airfoil's aerodynamic performance.

3.2.1. AFC parameters

Before deepening into the results of both parts of the AFC study, it is prime to be aware of the different synthetic jet parameters that determine the actuation setup. Firstly, it should be recalled that actuation is achieved by means of an oscillating membrane located right inside the airfoil's surface. Such actuation mechanism falls within the Zero Net Mass Flow Actuators (ZNMFA) category, also called Synthetic Jet Actuators (SJA), as it exchanges momentum with the boundary layer without any source or sink of external flow. Despite numerous actuation parameters exist, Synthetic Jet Actuators (SJA) can be characterized by the following set of five different parameters, namely the flow ejection/suction incident angle θ, the jet width h, the pulsating jet density ρ_j, the momentum coefficient associated with the pulsating jet C_μ, and the non-dimensional frequency F^+.

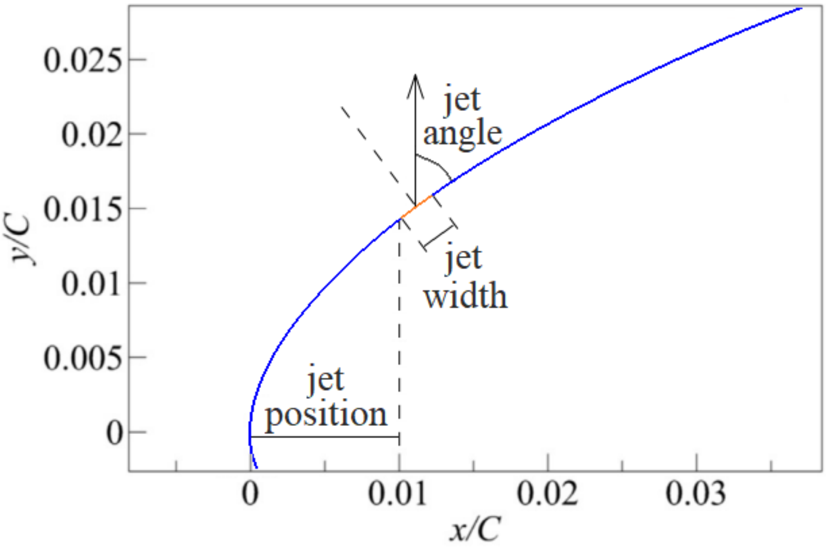

Figure 3.6: Synthetic jet geometrical parameters. Oscillating membrane (orange line) not to scale.

The flow ejection/suction incident angle is defined with respect to the airfoil's surface as sketched in figure 3.6. On the other hand, regarding the pulsating jet air density, following the same work principles as Tousi et al. [2], it is taken to be equal to the free-stream air density $\rho_j = \rho = 1$. In contrast to the previous parameters, the definition of the momentum coefficient associated with the pulsating jet is a bit more complex as it is derived from the momentum exchange between the boundary layer and the SJA, taking the following expression:

$$C_\mu = \frac{h\rho_j U_j^2 sin\theta}{C\rho U_\infty^2} \tag{3.1}$$

where U_j is the pulsating jet velocity. It is a common practice to characterize synthetic jets by their momentum coefficient rather than from their pulsating jet velocity. Even though they are directly related, the ultimate mechanism through which actuation is performed is via the exchange of momentum. Thus stating the direct value of such momentum is often preferred. To conclude, the fifth parameter, the non-dimensional frequency, is directly defined via the following expression:

$$F^+ = \frac{fC}{U_\infty} \tag{3.2}$$

where f is the dimensional frequency at which the membrane oscillates. Lastly, with the SJA characterized by these five parameters, its physical behavior is recreated inside the numerical setup by imposing oscillating Dirichlet boundary conditions for velocity and Neumann boundary conditions for pressure on the jet patch. The expression for such oscillating velocity boundary conditions takes the following form:

$$u_j = U_j sin(2\pi f t) \tag{3.3}$$

where U_j is the maximum jet velocity obtained from the jet-associated momentum coefficient.

3.2.2. Optimum SJA parameters

In this first part of the actuated study, the SJA optimum parameters for both maximum lift and aerodynamic efficiency cases found by Tousi et al. [2] are employed to assess the performance of the study's actuated numerical setup. Similar to the baseline case, addressing the reliability of the actuation setup will ensure the integrity of the results in the second part of the actuated study.

The SJA and the resulting mean aerodynamic performance parameters obtained by Tousi et al. [2] are displayed in table 3.2. To reach these maximized aerodynamic coefficients in terms of C_l and η, Tousi et al. conducted an optimization process via Genetic algorithms (GA), which consisted of up to 600 actuated cases. To deal with such an elevated number of simulations, the process was automatized by producing new SJA parameters according to the feedback from the GA optimizer and fed into a mesh generator that developed a new mesh for the updated case. This way, a notorious number of SJA parameter configurations could be tested until finding those that maximized either the lift C_l or the aerodynamic efficiency η.

Table 3.2: Maximized SJA parameters and its resulting mean aerodynamic performance coefficients obtained by Tousi et al. [2]

Cases	F^+	C_μ	θ°	x/C	h/C	C_l	C_d	η
Maximum lift	1.5	0.0051	44	0.0082	0.005	1.344	0.134	10.00
Maximum efficiency	2.4	0.0055	18	0.0097	0.005	1.170	0.085	13.70

It is safe to say that these maximized parameters produced a stunning boost in the airfoil's aerodynamic capabilities. Starting with the maximum lift case, Tousi et al. were able to raise the airfoil lift by an impressive $\Delta C_l/C_l = 68.36\%$ while improving the overall aerodynamic efficiency by $\Delta\eta/\eta = 156.41\%$. On the other hand, the maximum efficiency case reached an increase on the lift of $\Delta C_l/C_l = 46.64\%$ while $\Delta\eta/\eta = 251.28\%$ in the overall aerodynamic efficiency. Such results clearly show how adequate SJA active flow control is capable of enhancing the SD7003 baseline capabilities to a new level.

Unfortunately, to the author's surprise, the results obtained from applying the optimized parameters differed notably from those obtained by Tousi et al. [2]. Looking for an explanation for such deviation, the author found in the latest study conducted by Tousi et al. [6] that, in contrast to the baseline case where the choice of the modified turbulent viscosity $\tilde{\nu}$ boundary condition had little effect over the converged solution, it had a notable influence over the actuated cases.

Such was this influence that Tousi et al. decided to carry out a brief study assessing the sensitivity of the modified turbulent viscosity $\tilde{\nu}$ boundary condition across the baseline, maximum lift, and maximum efficiency cases over a range of modified turbulent viscosity values $\tilde{\nu}/\nu \in \left[10^{-20}, 10^{2}\right]$. Results for the baseline case showed that $\tilde{\nu}$, as mentioned before, had little to no effect over the converged solution since pretty identical results were obtained across the whole range of $\tilde{\nu}$ with the exception of unrealistically high values $(\tilde{\nu}/\nu \geq 1)$. However, in both actuated cases, the study showed significant discrepancies. Values low enough such as $\tilde{\nu}/\nu \sim 10^{-20}$ seemed to be artificially stabilizing the flow in the vicinities of the leading edge and thus inducing wrong results. On the other hand, high enough values such as $\tilde{\nu}/\nu \sim 1$ also produced results that lacked physical meaning. It was concluded that the values of $\tilde{\nu}$ that better matched LES results were those in the range of $\tilde{\nu}/\nu \in \left[10^{-6}, 10^{-3}\right]$, and a value of $\tilde{\nu}/\nu = 10^{-5}$ was employed to conduct further studies.

In addition, it was also found that when the previously thought maximized SJA parameters for both maximum lift and efficiency were tested using $\tilde{\nu}/\nu = 10^{-5}$, an overall optimal arose. Such optimal corresponded to the maximum efficiency case, which was capable of producing more lift than the presumed maximum lift case. In light of these findings and following Tousi et al. steps, a similar yet more modest modified turbulent viscosity study was conducted. In order to save days of computation, the range of $\tilde{\nu}$ was reduced from $\tilde{\nu}/\nu \in \left[10^{-20}, 10^{2}\right]$ to $\tilde{\nu}/\nu \in \left[10^{-15}, 1/3\right]$, which ensured that values around $\tilde{\nu}/\nu = 10^{-5}$ were well covered. The goals of this study were to evaluate the behavior of the previously thought optimum SJA parameters as a function of $\tilde{\nu}$, check whether a similar overall optimum arosed, and if so, compare it with Tousi et al. [6] LES results.

Table 3.3: Mean aerodynamic performance coefficients of the maximum lift SJA parameters across the several values of $\tilde{\nu}$.

Cases	C_l	C_d	η
$\tilde{\nu}/\nu = 1/3$	1.186	0.128	9.239
$\tilde{\nu}/\nu = 10^{-5}$	1.239	0.120	10.327
$\tilde{\nu}/\nu = 10^{-10}$	1.242	0.116	10.660
$\tilde{\nu}/\nu = 10^{-15}$	1.288	0.117	11.030

Table 3.4: Mean aerodynamic performance coefficients of the maximum aerodynamic efficiency SJA parameters across the several values of $\tilde{\nu}$.

Cases	C_l	C_d	η
$\tilde{\nu}/\nu = 1/3$	0.889	0.179	4.958
$\tilde{\nu}/\nu = 10^{-5}$	1.273	0.100	12.701
$\tilde{\nu}/\nu = 10^{-10}$	1.225	0.100	12.254
$\tilde{\nu}/\nu = 10^{-15}$	1.197	0.085	14.147

The resulting aerodynamic performance coefficients from the free-stream turbulence study show a clear dependence on the choice of this boundary condition. In the case of the maximum lift configuration, depicted in table 3.5, decreasing the value of $\tilde{\nu}$ results in supposedly better aerodynamic performances. Nevertheless, addressing the physical meaningfulness of these low values of $\tilde{\nu}$ has to be done via other aerodynamic properties such as the pressure coefficient or the skin friction coefficient distributions. On the other hand, in the case of the maximum efficiency shown in table 3.4, the best aerodynamic performance is achieved by $\tilde{\nu}/\nu = 10^{-5}$, which in accordance with the results obtained from Tousi et al. in their latest study [6], it consists of an absolute optimum that produces both higher lift and aerodynamic efficiency than the previously thought maximum lift configuration.

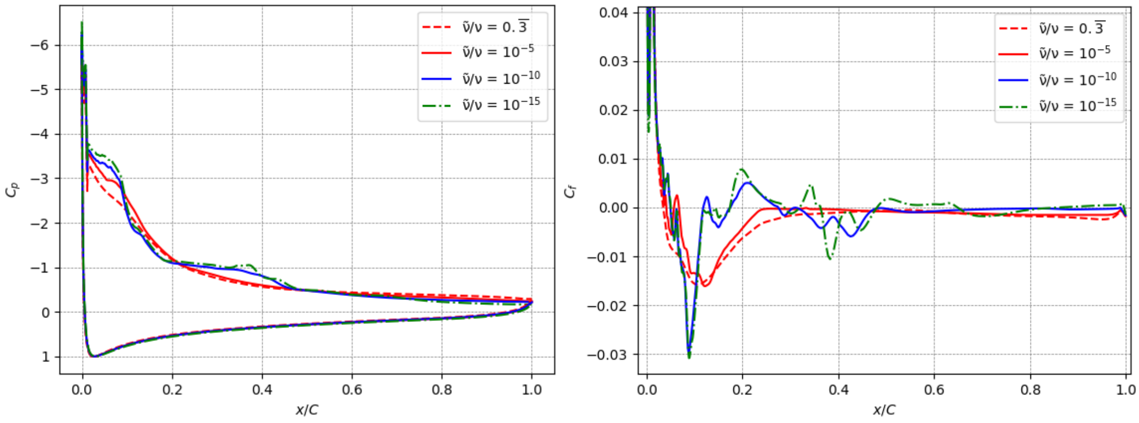

(a) (b)

Figure 3.7: Maximum lift configuration (a) pressure $C_p(x/C)$ and (b) skin friction $C_f(x/C)$ coefficient distributions from the several $\tilde{\nu}$ values.

Regarding the maximum lift configuration, the pressure distribution in the airfoil's lower surface shows no dependence on the value of $\tilde{\nu}$ as all four pressure distributions are, for all purposes, identical. On the other hand, portrayed in figure 3.7(a), several tendencies can be identified in the airfoil's upper surface for the different values of $\tilde{\nu}$. Lower values of $\tilde{\nu}$ retard the suction drop in the vicinities of the jet location, thus contributing to higher lift coefficients. However, they lead to higher adverse pressure gradients seen by the following boundary layer development, which by looking at the skin friction distribution in figure 3.7(b), small recirculating regions are developed as a consequence of such adverse pressure gradients. In contrast, for values of $\tilde{\nu}/\nu = 1/3$ and $\tilde{\nu}/\nu = 10^{-5}$, these recirculating regions are substituted by the early development of a separation bubble characterized by a null value of the skin friction coefficient. The pressure drag associated with this separation bubble seems to contribute to the higher drag coefficients of these latter values of $\tilde{\nu}$. Lastly, it is safe to say that lower values of $\tilde{\nu}$ lead to a more complex interaction with the boundary layer characterized by the formation of several small recirculating regions in the middle part of the chord, which all in all seem to prove beneficial for the airfoil's aerodynamic performance. Nevertheless, their physical meaningfulness is still yet to be addressed. Unfortunately, this task requires comparison with experimental or LES/DNS results for this SJA configuration, which at the moment of writing this document, such results are unavailable.

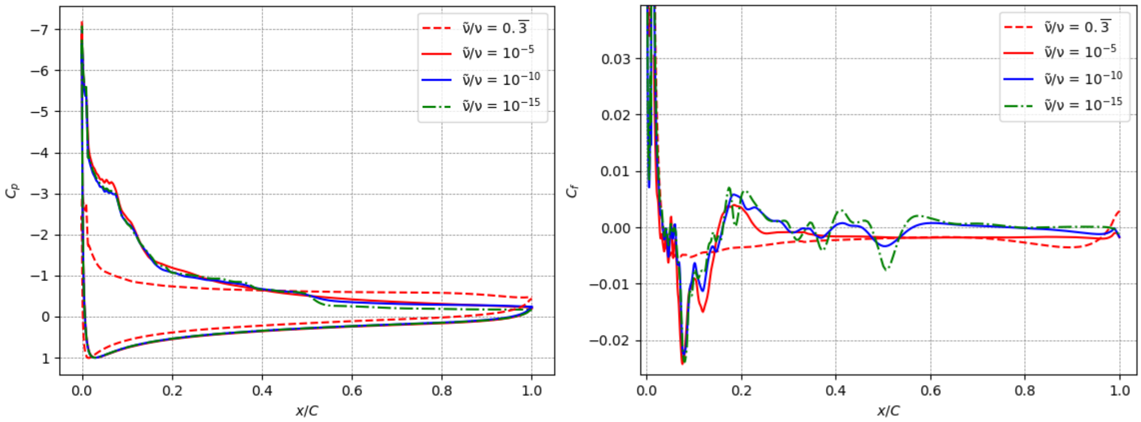

(a) (b)

Figure 3.8: Maximum efficiency configuration (a) pressure $C_p(x/C)$ and (b) skin friction $C_f(x/C)$ coefficient distributions from the several $\tilde{\nu}$ values.

Depicted in figure 3.8(a), the maximum efficiency configuration pressure distribution shows several differences between the four cases in both upper and lower airfoil surfaces. High values of $\tilde{\nu}$ clearly fail to capture correctly the interaction between the jet and the boundary layer as it is shown by both the pressure and skin friction distributions resembling more those from the baseline case than the ones from actuated cases. This inability to perform actuation properly entails the poor airfoil's aerodynamic performance, which is just slightly better than the baseline case one. On the other hand, once values of $\tilde{\nu}$ are low enough, at least $\tilde{\nu}/\nu \leq 10^{-5}$, they resolve the lower surface, for all purposes again, identically. In contrast, similar yet slightly different pressure and skin friction distributions can be seen on the upper surface. The value that reaches the highest suction zone in the jet vicinities is $\tilde{\nu}/\nu = 10^{-5}$, and lower values seem to behave similarly reaching lower suction zones in both cases. The subsequent adverse pressure gradient is essentially the same for all of them, although several differences can be noticed by looking at the skin friction distribution in figure 3.8(b). Values lower than $\tilde{\nu}/\nu \leq 10^{-10}$ generate several small recirculation regions across the middle chord while $\tilde{\nu}/\nu = 10^{-5}$ develops a separation bubble instead, which similarly to the previous configuration, it implies that lower values of $\tilde{\nu}$ lead to a more complex interaction with the boundary layer. However, in this case, $\tilde{\nu}/\nu = 10^{-5}$ leads to the best airfoil aerodynamic performance, which consists of an absolute optimum, just as Tousi et al. found in their latest study [6].

Table 3.5: Time-averaged aerodynamic performance coefficients of the absolute optimum and their respective errors with respect to the values found in the literature.

Cases	C_l	ε_{C_l}	C_d	ε_{C_d}	η	ε_η
Present - SA	1.273	-	0.100	-	12.701	-
Tousi et al. - SA	1.288	-1.16%	0.097	+3.09%	13.27	-4.29%
Tousi et al. - LES	1.313	-3.05%	0.094	+6.38%	13.96	-9.02%

In contrast to the maximum lift configuration case, RANS and LES results depicting both the pressure and the skin friction coefficient distributions are available for these specific SJA parameters, concretely the ones obtained by Tousi et al. [6]. A comparison with these results shows that the overall optimum found in the modified turbulent viscosity sensitivity study is in close agreement with the ones obtained by Tousi et al. in their latest study, especially with the RANS one. In the case of the lift coefficient, minute errors of $\varepsilon_{RANS} = -1.16\%$ and $\varepsilon_{LES} = -3.05\%$ are obtained when compared to the values achieved by Tousi et al. for such optimum via RANS and LES simulations, respectively. As for the drag coefficient, slightly higher errors of $\varepsilon_{RANS} = +3.09\%$ and $\varepsilon_{LES} = +6.38\%$ are observed. Lastly, as the errors can be amplified in the case of the aerodynamic efficiency, errors of $\varepsilon_{RANS} = -4.29\%$ and $\varepsilon_{LES} = -9.02\%$ are derived from the previous two coefficients. All in all, the obtained aerodynamic performance of the absolute optimum matches nicely the values available in the literature. However, as seen on previous occasions, as aerodynamic force coefficients can be misleading due to compensations across the chord, the pressure and skin friction coefficient distributions should be analyzed to obtain meaningful comparisons.

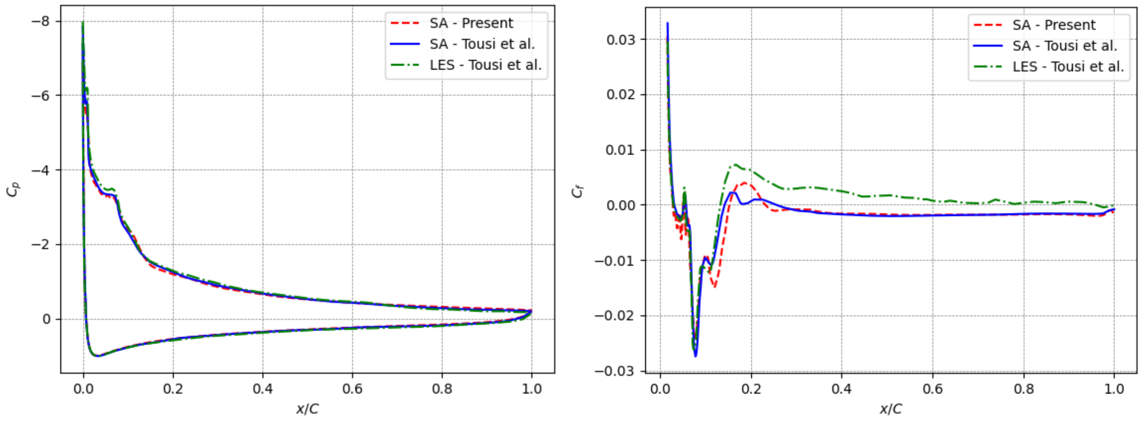

(a) (b)

Figure 3.9: Absolute optimum (a) pressure $Cp(x/C)$ and (b) skin friction $Cf(x/C)$ coefficient distributions comparison with the literature.

An analysis of the pressure coefficient distribution reveals that the results obtained in the free-stream study match outstandingly not only RANS results obtained by Tousi et al. but also LES ones as well. Presented in figure 3.9(a), all three distributions behave identically, except for a small region in the suction zone in the vicinities of the jet where the LES distribution reaches higher suctions, thus contributing to its higher lift coefficient. In contrast, depicted in figure 3.9(b), the skin friction coefficient presents several dissimilarities between the three distributions. RANS results are in close agreement with LES ones in the initial chord section but fail to reproduce their behavior in the latter parts of the chord. Nevertheless, all three distributions indicate that the flow reattaches around $x/C \approx 0.15$, from where LES results maintain the flow attached across the remaining chord, thus contributing to its lower drag coefficient. In contrast, RANS distributions show that the flow separates briefly after reattaching to maintain a negative but close to zero value for the rest of the chord, which seems to have no severe pressure drag penalty as their drag coefficients are pretty close to the LES one. The stunning agreement in the case of the pressure coefficient distribution and the similar traits presented by the skin friction coefficient distribution, not only prove the integrity of the study's actuated numerical setup but also that the Spalart-Allmaras turbulence model is capable of capturing the flow behavior properly when no such separated flows are present, providing that its parameters are well tuned. To conclude, in light of the results obtained from this first part of the AFC study, a modified turbulent viscosity value of $\tilde{\nu}/\nu = 10^{-5}$ has been chosen to conduct the rest of the simulations.

3.2.3. Tangential jet configuration

In this second part of the actuated study, a tangential synthetic jet was employed to perform actuation over an SD7003 airfoil, which to the best of the author's knowledge, was the first time this approach was taken over an SD7003 airfoil. In spite of the findings by Tousi et al. in both of their studies [2] [6], which pointed out that reducing the jet incident angle led to higher aerodynamic efficiencies, the author was pleased to address this statement in this document.

3.2.3.1. Mesh adaptation

The implementation of the tangential synthetic jet required changing the airfoil's geometry. Sketched in figure 3.11, the oscillating membrane was placed perpendicularly to the airfoil's surface in the corresponding jet location. In order to allow the flow to exit the jet patch smoothly to the upper airfoil's surface, an indent in the airfoil's profile had to be made. Nonetheless, performing such an indent only required adding a few auxiliary points during the mesh development process.

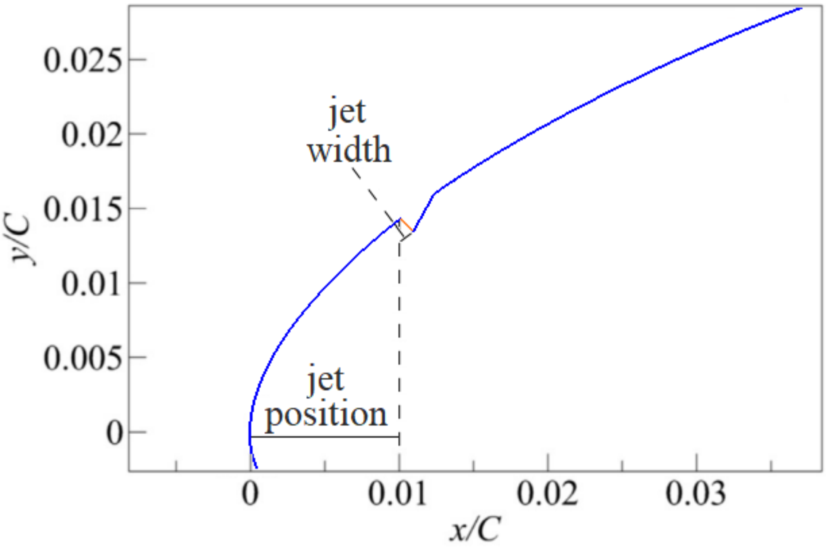

Figure 3.10: Tangential synthetic jet implementation into the airfoil's geometry. Oscillating membrane (orange line) not to scale.

In contrast, as the closest region of the computational domain mesh was composed of structured cells, meshing the resulting geometry demanded making several modifications to the mesh topology. Since structured meshing cannot be applied to triangular regions, an auxiliary meshing region, illustrated in figure 3.11, that extended up to the very trailing edge section had to be placed in order to keep the closest region meshed with structured cells. Nevertheless, this implementation process was a one-time work since the python meshing engine, first presented in section 2.2., was updated so that the development of the tangential jet's mesh was done automatically. In addition, in order to maintain the resolution and homogeneity of the cells in the vicinities of the surface, the presence of this new auxiliary region increased the total number of cells within the mesh from 76186 to 91278. Nevertheless, such an increase in no case was prohibitive and just ended up slightly rising the computational requirements of the study.

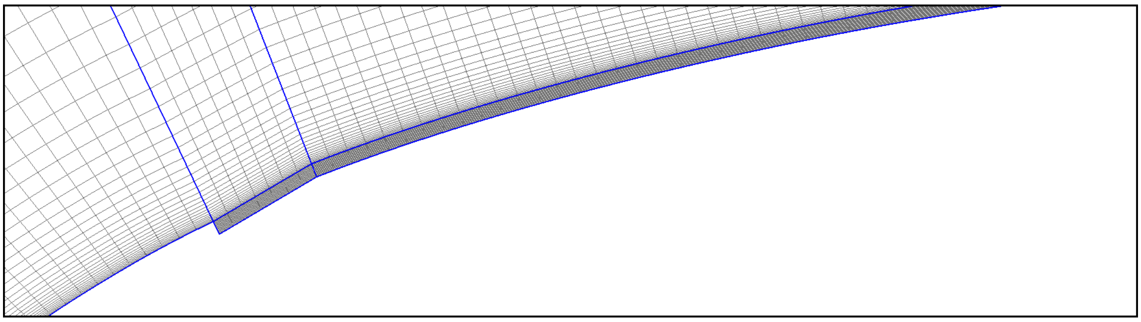

Figure 3.11: Tangential synthetic jet auxiliary region (dark grey) and closest region (light grey) of the adapted mesh.

3.2.3.2. Actuation parameters

Regarding the actuation parameters, several aspects have to be considered before defining the corresponding boundary conditions. As mentioned in the introduction of this second part of the actuated study, incident angles that tend towards tangency produce higher aerodynamic efficiencies. For this reason, the author decided to conduct this study with a value of the momentum coefficient corresponding to the absolute optimum found in section 3.2.2., namely $C_\mu = 0.0055$. On the other hand, as the jet incidence angle is now fixed to 90°, there is a reduction in the degrees of freedom to produce different actuation configurations. Recalling the momentum coefficient mathematical definition:

$$C_\mu = \frac{h\rho_j U_j^2 sin\theta}{C\rho U_\infty^2} \tag{3.4}$$

It is straightforward to see that there are only four remaining actuation parameters left to produce different actuation configurations, namely the jet width h/C, the maximum jet velocity U_j, the non-dimensional frequency F^+, and the jet location x/C. In fact, by applying the corresponding jet and flow values to the variables of the previous equation, it reduces to the following expression:

$$hU_j^2 = 0.0055 \tag{3.5}$$

This equation states that the jet width h and the maximum jet velocity U_j are related to each other in order to produce the desired momentum coefficient. Nevertheless, both the jet width and the maximum jet velocity, are bounded by physical constraints. On the one hand, the jet width has to be sufficiently small so that the slope of the indent, shown in figure 3.11, is smooth enough to avoid becoming a kind of semi-jet that sends the flow perpendicularly to the boundary layer. On the other hand, the maximum jet velocity also has to be maintained low enough as high values would be impossible to produce by an oscillating membrane. For the aforementioned reasons, two appropriate arbitrary values for both parameters that fulfill the previous equation and ensure physical meaningfulness have been chosen as $h/C = 0.0005$ and $U_j = 3.317\ m/s$.

Regarding the two remaining actuation parameters, different values of both the non-dimensional frequency F^+ and the jet location x/C have been considered to conduct this study. Concretely, three different non-dimensional frequencies $F^+ = \{1, 1.5, 2\}$ applied in two different jet locations $x/C = \{0.0082, 0.0097\}$, which correspond to the jet locations of the maximum lift and aerodynamic efficiency cases found by Tousi et al. [2], making up a total of six actuated configurations.

3.2.3.3. Results

The results obtained from the simulations of all six actuated cases show promising improvements in the airfoil's aerodynamic performance. Presented in table 3.6, their resultant mean aerodynamic performance parameters show pretty respectable improvements in both lift and aerodynamic efficiency coefficients with respect to the baseline case. Despite a maximum lift coefficient improvement of $\Delta C_l^{max}/C_l = +49.88\%$ for the 'Actuated 5' case and a maximum aerodynamic efficiency improvement of $\Delta\eta^{max}/\eta = +167.31\%$ for 'Actuated 6', all five converged solutions show stunning performances reaching minimum improvements of of $\Delta C_l^{min}/C_l = +47.91\%$ and $\Delta\eta^{min}/\eta = +133.33\%$ for the 'Actuated 2' and 'Actuated 4', respectively. Such similar high values of the coefficient improvements make it hard to identify any trend towards an optimum in neither lift nor aerodynamic efficiency terms, especially since only six cases have been addressed. Nevertheless, analyzing the flow dynamics of the cases providing the highest improvements might help identify the actuation behaviors that are most beneficial for improving the airfoil's aerodynamic capabilities.

Table 3.6: Mean aerodynamic performance coefficients of the actuated cases and lift and aerodynamic efficiency coefficient improvements with respect to the baseline case.

Case	F^+	x/C	C_l	C_d	η	$\Delta C_l/C_l$	$\Delta\eta/\eta$
Actuated 1	1	0.0082	1.212	0.124	9.762	+48.89%	+141.04%
Actuated 2	1.5	0.0082	1.204	0.116	10.336	+47.91%	+155.21%
Actuated 3	2	0.0082	-	-	-	-	-
Actuated 4	1	0.0097	1.210	0.128	9.456	+48.65%	+133.33%
Actuated 5	1.5	0.0097	1.220	0.115	10.605	+49.88%	+161.85%
Actuated 6	2	0.0097	1.207	0.111	10.826	+48.28%	+167.31%
Optimal 3.5	2.4	0.0097	1.273	0.100	12.701	+56.39%	+213.60%

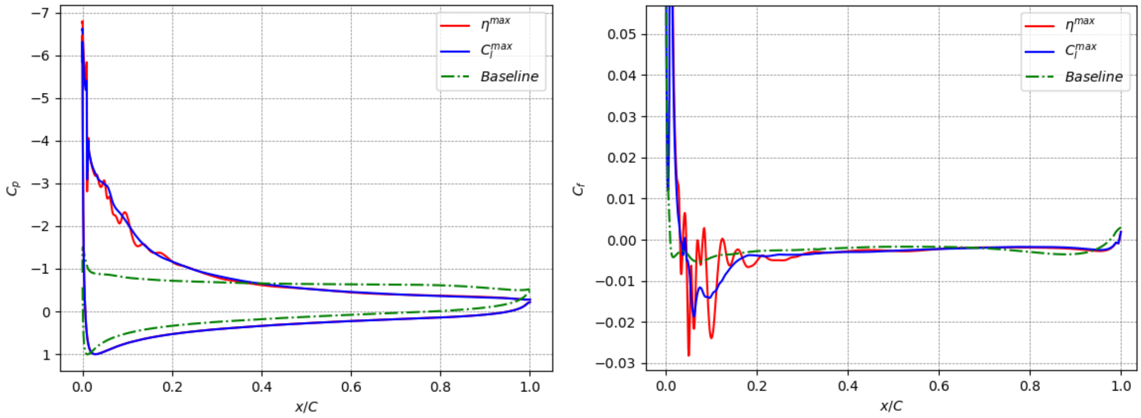

(a)

(b)

Figure 3.12: Maximum efficiency (red line), maximum lift (blue line), and baseline (green line) cases (a) pressure $Cp(x/C)$ and (b) skin friction $Cf(x/C)$ coefficient distributions.

Comparing the best performing actuated cases' pressure and skin friction coefficients with those from the baseline case exposes some of the numerous benefits of its actuation. Portrayed in figure 3.12, both maximum lift and aerodynamic efficiency cases show identical values of the pressure distribution in both upper and lower surfaces, except for the region located in the first upper surface's early chord. In this region, the maximum efficiency case presents an oscillatory behavior around the distribution of the maximum lift coefficient, which resembles the tendency found in the modified turbulent viscosity study. Nevertheless, both cases expose the clear benefits of AFC over the baseline distribution, even at the lower surface, where higher pressures are reached across the entire chord. As for the skin friction coefficient distributions, similar yet different behaviors are found in both actuated cases. Similar to the pressure distribution, the maximum efficiency case fluctuates around the value of the maximum lift case. Nevertheless, both of them succeed equally in retarding separation, as shown by the latter change in the sign of the skin friction coefficient when compared to the baseline case.

Nevertheless, before deepening further in their analysis, the behavior of one of the actuated cases should be addressed. Among the several actuated cases presented in table 3.6, the 'Actuated 3' case failed to perform actuation properly, as it seemed to override the effects of any beneficial trait of AFC. This configuration developed recirculating regions with such a high frequency that the fluctuations these caused in the boundary layer velocity field ended up generating a large separation bubble similar to the one of the baseline case, thus resulting in poor actuation performance.

The time evolution of the lift coefficient presented in figure 3.13 clearly shows the effects of such fluctuating behavior. Initially, the 'Actuated 3' case produced outstanding values of the instantaneous lift coefficient, however, as the flow evolved, the fluctuations caused by the recirculating regions propagating down the upper's surface started growing leading to a gradual degradation of its value, until at some point around 25-time units, they were so pronounced that ended up completely destabilizing the boundary layer leading to a massive drop of the lift coefficient.

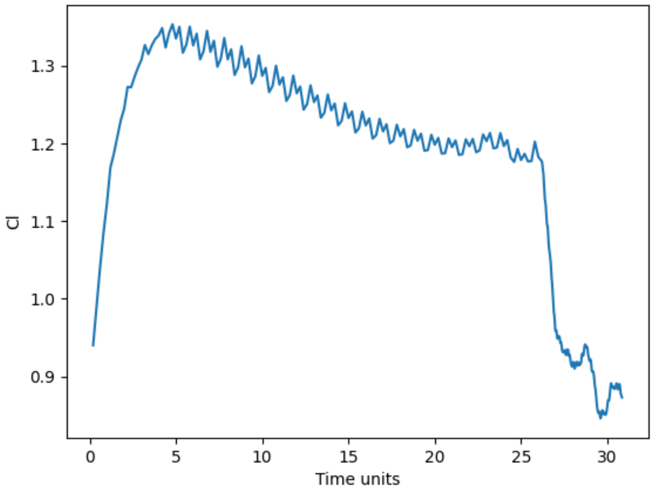

Figure 3.13: Lift coefficient time evolution of the 'Actuated 3' case.

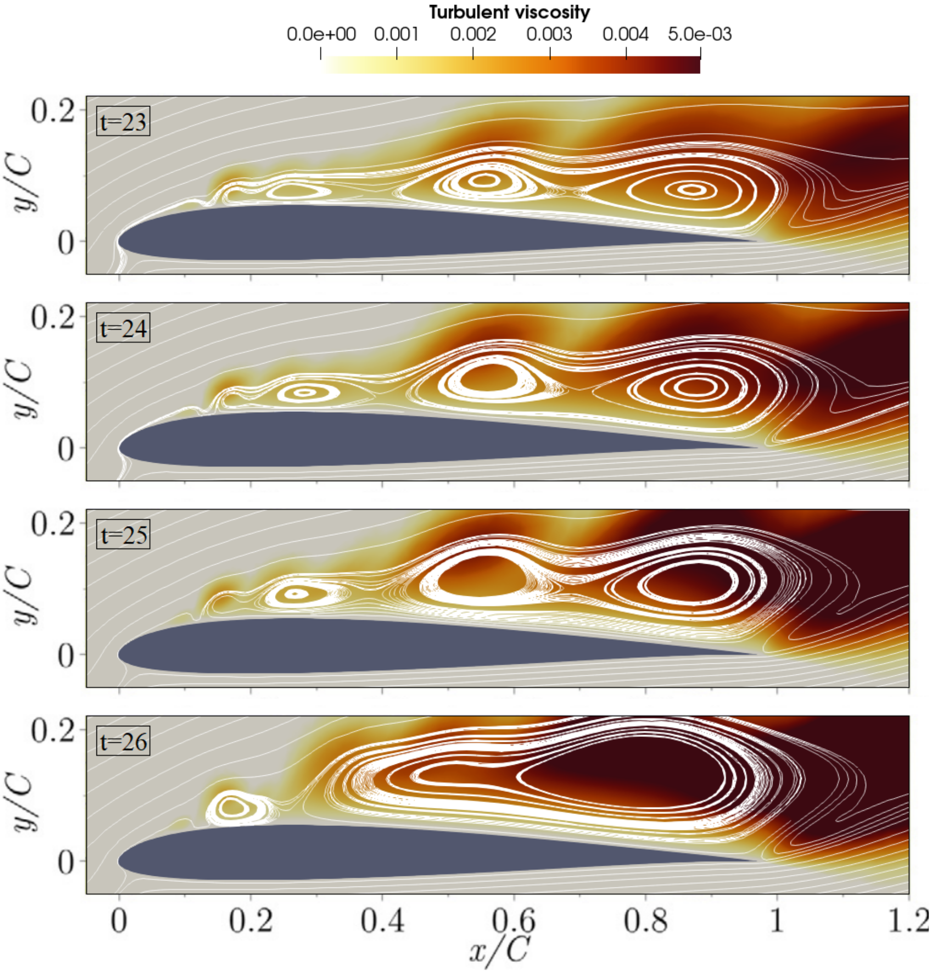

Figure 3.14: Destabilization of the boundary layer field caused by the fast production of recirculating regions across time units 23, 24, 25, and 26 pictured from top to bottom, respectively.

Figure 3.14 presents four different stages of the flow evolution, concretely at 23, 24, 25, and 26 time units. In its captions, not only the growth of the several recirculating regions can be seen due to a stroboscopic effect ($T_{jet} = 0.5$ s), but also the merging of two of these regions into the previously mentioned large separation bubble. In addition, by looking at the contour lines of the turbulent viscosity, it can be appreciated how turbulence is enhanced as the boundary layer is destabilized.

Several conclusions can be made from this tangential jet configuration study. Firstly, as seen by the 'Actuated 3' case's destabilization of the boundary layer and the fluctuating behavior of the pressure and skin friction coefficients of the maximum efficiency case, in this synthetic jet configuration the value of the non-dimensional frequency plays a crucial role in the interaction between the jet and the boundary layer. Higher frequencies are able to produce numerous recirculating regions that propagate over the upper airfoil's surface which, as seen with the 'Actuated 3' case, can lead to suppressing all effects of actuation by destabilizing the boundary layer.

In contrast, lower values of the non-dimensional frequency interact in a simpler manner with the boundary layer, which results in a more 'safe' actuation regarding its destabilization. Similar behaviors in the interaction with the boundary layer like the ones between the different frequencies were also noticed during the turbulent viscosity sensitivity study, where lower values of $\tilde{\nu}$ led to complex interactions and the production of several recirculating regions.

Lastly, despite no actuated case tested in this second part of the AFC study achieved a better aerodynamic performance than the one of the absolute optimal found in the sensitivity study, the tangential SJA approach showed promising results. A modest study consisting of six actuated cases has been able to produce notorious improvements, which are not in any case far from the ones of the absolute optimum found with the previous synthetic jet approach, especially for the lift. For this reason, although there has not been any clear sign of this approach producing notoriously high aerodynamic efficiencies, it has proved that it is very capable of performing actuation at a high level.

CONCLUSIONS

After an initial extensive pre-processing stage where the quality of the numerical setup mesh was addressed in order to reach a design that best fitted the computational resources available while providing the maximum degree of accuracy possible, numerous findings have been encountered across the entirety of this bachelor thesis. As for the mesh itself, a hybrid mesh consisting of structured cell regions in the airfoil's vicinity and unstructured cell regions in the rest of the computational domain proved to be the best approach to reach an adequate balance between accuracy and computational resources.

The resolution of the baseline case via RANS turbulence models exposed the inability of turbulent kinetic energy models, specifically of $Realizable-k-\varepsilon$ and $SST-k-\omega$ models, to solve large separated flows like those encountered in post-stall regimes, making clear that for high values of the angle of attack, the choice of the turbulence model employed is vital. Nevertheless, it might be possible that provided a proper tuning of their model parameters or a modification in their model equations is performed, they can end up solving such separated flows.

In spite of such further treatment which in no case is a guarantee of a successful outcome, they both have not been considered to conduct the actuated studies performed later on. In addition, the stunning performance that the Spalart-Allmaras displayed in the baseline case, proved that it was capable of dealing with further actuated cases. Nevertheless, it was made clear that it underestimates both aerodynamic force coefficients, especially for the drag, which was always below the values found by LES simulations. However, considering the reduced computational resources it required in comparison to LES, its performance can be denoted as excellent since, in most cases, it provided errors more than acceptable for the considered flow regime.

A maximum error of $\varepsilon^{max} = 3.58\%$ was obtained in the baseline case when comparing the aerodynamic performance parameters with those of RANS results available in the literature. In contrast, a noticeable maximum error of $\varepsilon^{max} = -15.89\%$ was obtained when compared with LES results. In addition, a laminar boundary layer separation was found to take place at $x/C = 0.015$, which is well within the values found in the literature. All in all, the flow dynamics were well captured, revealing a large recirculating region over the upper airfoil's surface and a smaller one on the trailing edge.

The conduction of a sensitivity study with respect to the turbulent viscosity employed in the Spalart-Allmaras model showed a clear dependence of the results on the choice of this value, which exposed the flaw that turbulence models often depend on appropriate parameter tuning to perform appropriately. Furthermore, such dependence uncovered the difficulty to conduct an optimization process of SJA parameters, as there is no guarantee that the same value of $\tilde{\nu}$ would be capable of capturing the flow dynamics across the different ranges of scenarios faced in such optimization processes.

From this study was also concluded that the value that captured best the flow dynamics obtained with LES results was $\tilde{\nu}/\nu = 10^{-5}$, which when compared to RANS and LES results found in the literature, an outstanding agreement between them was found. This agreement, especially with LES results, proved that the Spalart-Allmaras model is capable of performing with a high degree of accuracy provided that its model parameters are well adjusted and such separated flows like the one of the baseline case are no longer present.

Furthermore, the aerodynamic performance improvements of the optimal set of SJA parameters found in the sensitivity study were notorious, reaching impressive improvements of $\Delta C_l/C_l = 56.39\%$ and $\Delta\eta/\eta = 213.60\%$ for the lift coefficient and the aerodynamic efficiency, respectively.

The last AFC study addressed the actuation performance of a tangential jet approach implementation. The results proved this approach as promising as only by simulating six actuated cases, aerodynamic performance improvements over the baseline case were close to those of the optimal found in the turbulent viscosity sensitivity study. On top of that, the study exposed that the role of the non-dimensional frequency becomes crucial to destabilizing the boundary layer in this jet configuration, as higher frequencies introduce severe fluctuations within the boundary layer velocity field by the fast generation of recirculating regions that propagate across the upper surface.

In light of all the conclusions and outcomes found during the realization of this bachelor thesis, several lines of future work are proposed. Firstly, addressing the angle of attack range of applicability over an SD7003 airfoil of the turbulent kinetic energy turbulence models selected in the study and their dependence on their respective model parameters. This study could result fruitful in comparing their accuracy with the one of the Spalart-Allmaras to address whether they prove a better option at pre-stall regimes.

Secondly, as seen in the study of the turbulent viscosity sensitivity, further assessment of the influence of this value over a large range of SJA parameters is required in order to be able to conclude whether Spalart-Allmaras optimization processes are feasible or not. As a result, performing a sensitivity study for numerous SJA parameters could help identify how and under which circumstances the choice of the turbulent viscosity value becomes crucial.

Finally, the implementation of a tangential synthetic jet proved to reduce the range of SJA possible parameter values, as physical constraints in both the membrane and the jet width were present. Nevertheless, the slope connecting the synthetic jet and the airfoil upper surface can be studied as an extra SJA parameter, since depending on its inclination the slope itself can end up acting as a semi-jet, changing the orientation of the fluid being injected/sucked. For this reason, addressing the slope's influence over the AFC aerodynamic improvements can give an insight into richer actuation phenomena.

BIBLIOGRAPHY

[1] Louis N. Cattafesta and Mark Sheplak. Actuators for active flow control. *Annual Review of Fluid Mechanics*, 43:247–272, 2011. 1

[2] N.M. Tousi, M. Coma, J.M. Bergadà, J. Pons-Prats, F. Mellibovsky, and G. Bugeda. Active flow control optimisation on sd7003 airfoil at pre and post-stall angles of attack using synthetic jets. *Applied Mathematical Modelling*, 98:435–464, 2021. 2, 19, 25, 34, 35, 38, 39, 40, 41, 42, 46, 48

[3] P Catalano and R Tognaccini. Rans analysis of the low-reynolds number flow around the sd7003 airfoil. *Aerospace Science and Technology*, 15(8):615–626, 2011. 2, 28, 34, 36

[4] Michael Breuer. Effect of inflow turbulence on an airfoil flow with laminar separation bubble: An les study. *Flow, Turbulence and Combustion*, 101, 2018. 2

[5] Ivette Rodriguez, Oriol Lehmkuhl, and Ricard Borrell. Effects of the actuation on the boundary layer of an airfoil at reynolds number re= 60000. *Flow, Turbulence and Combustion*, 105:607–626, 2020. 2, 19, 35

[6] N.M. Tousi, J.M. Bergadà, and F. Mellibovsky. Large eddy simulation of optimal synthetic jet actuation on a sd7003 airfoil in post-stall conditions. *Aerospace Science and Technology*, 127, 2022. 2, 19, 34, 35, 38, 42, 43, 44, 46

[7] Frank M White. *Fluid mechanics*. Tata McGraw-Hill Education, 1979. 5

[8] J.D. Anderson. *Computational Fluid Dynamics*. McGraw-Hill Education, 1995. 5

[9] Stephen B Pope and Stephen B Pope. *Turbulent flows*. Cambridge university press, 2000. 9, 10, 11

[10] David C Wilcox et al. *Turbulence modeling for CFD*, volume 2. DCW industries La Canada, CA, 1998. 11

[11] Philippe Spalart and Steven Allmaras. A one-equation turbulence model for aerodynamic flows. In *30th aerospace sciences meeting and exhibit*, page 439, 1992. 12, 29

[12] Law of the wall, accessed 8 september 2022. `https://en.wikipedia.org/wiki/Law_of_the_wall`. 14

[13] J.D. Anderson. *Fundamentals of Aerodynamics*. McGraw-Hill, 2001. 14, 16, 17, 18

[14] Gmsh documentation, accessed 8 september 2022. `https://gmsh.info/`. 20

[15] Hand-made meshing script, accessed 8 september 2022. `https://github.com/Pedro-Munoz-Hoyos/Mesh-engine`. 20

[16] J. Tu, G.H. Yeoh, and C. Liu. *Computational Fluid Dynamics: A Practical Approach*. Elsevier Science, 2012. 23

[17] Openfoam incompressible flow solvers, accessed 8 september 2022. https://www.openfoam.com/documentation/guides/latest/api/group__grpIncompressibleSolvers.html. 27

[18] Openfoam k-epsilon, accessed 8 september 2022. https://www.openfoam.com/documentation/guides/latest/doc/guide-turbulence-ras-k-epsilon.html. 28

[19] Openfoam k-omega (sst), accessed 8 september 2022. https://www.openfoam.com/documentation/guides/latest/doc/guide-turbulence-ras-k-omega-sst.html. 28

[20] Paraview overview and its history, accessed 8 september 2022. https://www.paraview.org/overview/. 29

[21] Openfoam functionobjects, accessed 8 september 2022. https://www.openfoam.com/documentation/guides/latest/api/group__grpFunctionObjects.html. 30

[22] Openfoam running applications in parallel, accessed 8 september 2022. https://www.openfoam.com/documentation/user-guide/3-running-applications/3.2-running-applications-in-parallel. 30

APPENDICES

APPENDIX A. EXTRA AUDIOVISUAL MATERIAL

Video of the converged state solution of the **absolute optimum case** from the sensitivity study: `https://youtu.be/V0VIs9NraO0`

Video of the converged state solution of the **maximum lift case** from the tangential jet study: `https://youtu.be/q5QX5xUHl8c`

Video of the converged state solution of the **maximum efficiency case** from the tangential jet study: `https://youtu.be/Z1klAnFCnmA`

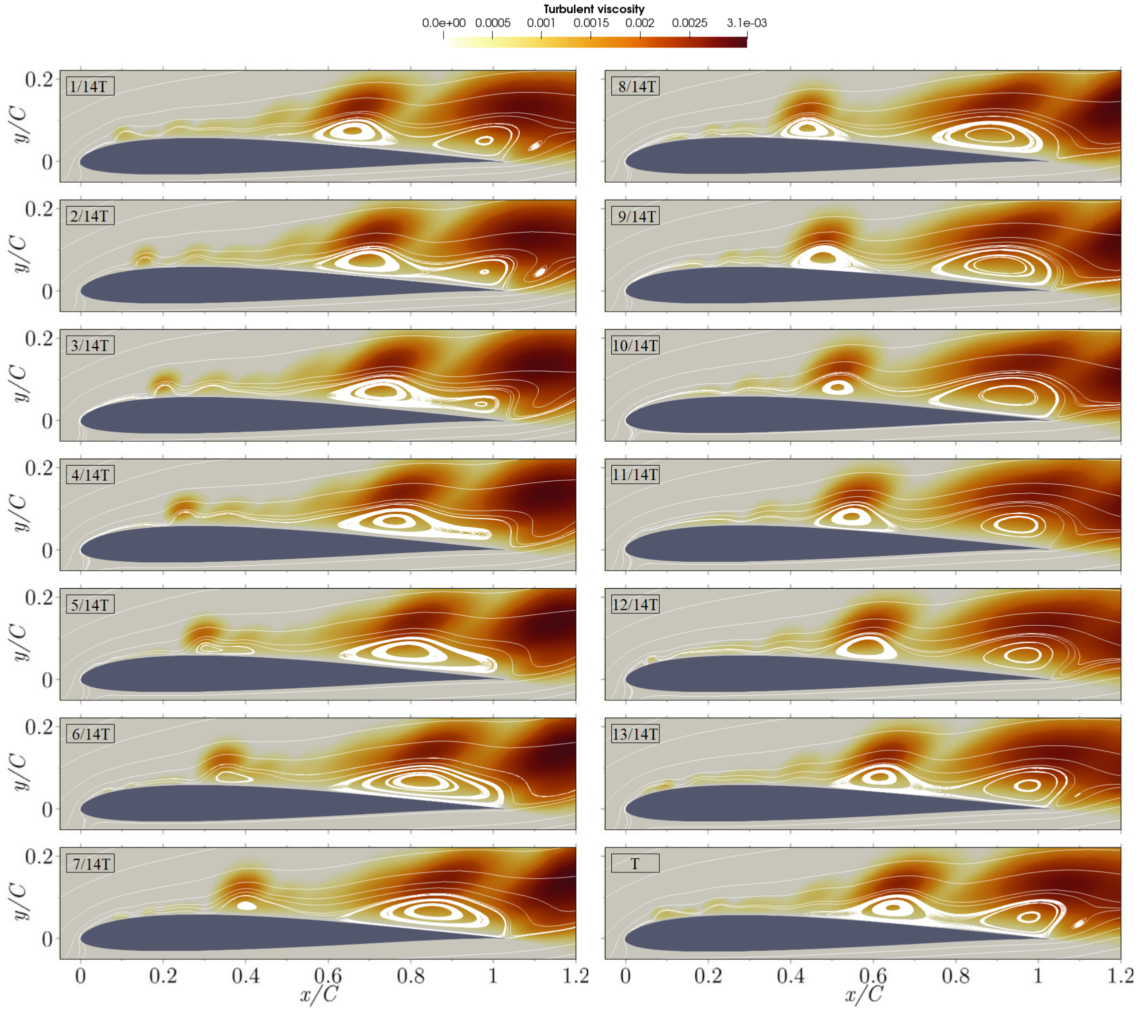

Figure A.1: Tangential study maximum lift case streamlines evolution over an actuation period.

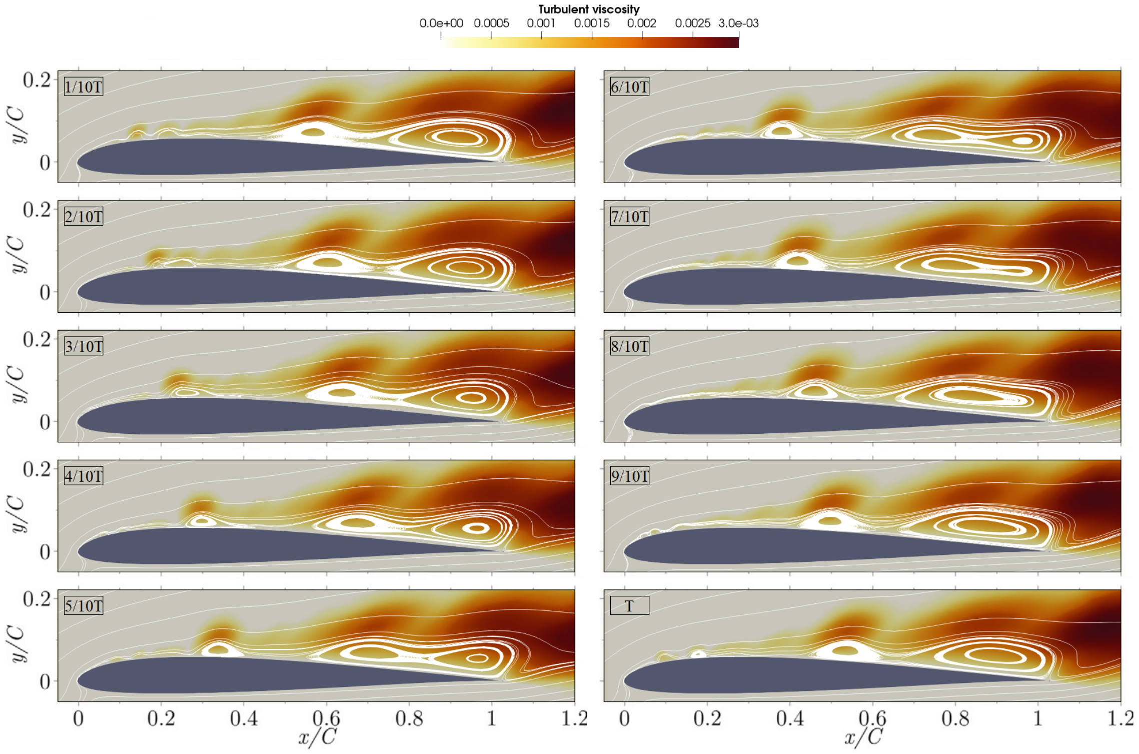

Figure A.2: Tangential study maximum efficiency case streamlines evolution over an actuation period.